

Infrared observations of hot gas and cold ice toward the low mass protostar Elias 29^{*}

A.C.A. Boogert^{1,2,3}, A.G.G.M. Tielens^{1,2}, C. Ceccarelli⁴, A.M.S. Boonman⁵, E.F. van Dishoeck⁵, J.V. Keane¹, D.C.B. Whittet⁶, and Th. de Graauw²

¹ Kapteyn Astronomical Institute, P.O. Box 800, 9700 AV Groningen, the Netherlands

² SRON, P.O. Box 800, 9700 AV Groningen, the Netherlands

³ Present address: California Institute of Technology, Downs Laboratory of Physics 320-47, Pasadena, CA 91125, USA

⁴ Laboratoire d'Astrophysique de l'Observatoire de Grenoble, B.P. 53X, 38041 Grenoble Cedex, France

⁵ Leiden Observatory, P. O. Box 9513, 2300 RA Leiden, the Netherlands

⁶ Department of Physics, Applied Physics & Astronomy, Rensselaer Polytechnic Institute, Troy, NY 12180, USA

Received 28 February 2000/ Accepted April 2000

Abstract. We have obtained the full 1-200 μm spectrum of the low luminosity ($36 L_{\odot}$) Class I protostar Elias 29 in the ρ Ophiuchi molecular cloud. It provides a unique opportunity to study the origin and evolution of interstellar ice and the interrelationship of interstellar ice and hot core gases around low mass protostars. We see abundant hot CO and H₂O gas, as well as the absorption bands of CO, CO₂, H₂O and “6.85 μm ” ices. We compare the abundances and physical conditions of the gas and ices toward Elias 29 with the conditions around several well studied luminous, high mass protostars. The high gas temperature and gas/solid ratios resemble those of relatively evolved high mass objects (e.g. GL 2591). However, none of the ice band profiles shows evidence for significant thermal processing, and in this respect Elias 29 resembles the least evolved luminous protostars, such as NGC 7538 : IRS9. Thus we conclude that the heating of the envelope of the low mass object Elias 29 is qualitatively different from that of high mass protostars. This is possibly related to a different density gradient of the envelope or shielding of the ices in a circumstellar disk. This result is important for our understanding of the evolution of interstellar ices, and their relation to cometary ices.

Key words: Stars: formation – individual: Elias 29 – ISM: dust, extinction – molecules – abundances – Infrared: ISM: lines and bands

1. Introduction

The general picture of low mass star formation has been formed since the 1980's with the availability of infrared and millimeter wavelength broad band photometry from the ground, and with the IRAS satellite and KAO observatory (e.g., Lada & Wilking 1984; Adams et al. 1987; Hillenbrand et al. 1992; André et al. 1993). A classification scheme was made, where the continuum emission of Class 0 and I objects peaks in the submillimeter and far-infrared. These objects are still deeply embedded in their accreting envelopes. In the Class II phase, the wind of the protostar has cleared its surrounding environment, such that it becomes optically visible, and shows H I emission lines. The continuum emission of these objects peaks in the near-infrared, but there is still significant excess emission above the stellar continuum. They are believed to be surrounded by optically thick dusty disks. Finally, little dust emission remains for Class III objects, when the disk is optically thin, and planetary companions may have been formed.

Our knowledge of the physical and chemical state and evolution of the material surrounding protostars, has progressed with the availability of medium and high resolution spectroscopic instrumentation at near and mid-infrared wavelengths ($\sim 2 - 20 \mu\text{m}$). The progress made, is best illustrated by the observations of high mass protostars, which are bright and easy to observe. The (ro-)vibrational bands of various molecules (CO, H₂O, CH₃OH, silicates) were observed from the ground, revealing profile variations of the 3.07 μm , and 4.67 μm H₂O and CO ice bands (e.g. Smith et al. 1989; Tielens et al. 1991; Chiar et al. 1998). This was interpreted as evaporation of the volatile CO ice, and crystallization of H₂O ice in the molecular envelopes. This heating effect is strengthened by the detection of hot gas in 4.6 μm CO

Send offprint requests to:

A.C.A. Boogert (boogert@submm.caltech.edu)

* Based on observations with ISO, an ESA project with instruments funded by ESA Member States (especially the PI countries: France, Germany, the Netherlands and the United Kingdom) and with the participation of ISAS and NASA.

observations (Mitchell et al. 1991). With the launch of the *Infrared Space Observatory* in 1995 (ISO; Kessler et al. 1996), it became possible to observe all other molecular bands in the infrared (Whittet et al. 1996). It was shown that high mass protostellar evolution can be traced in the gas-to-solid abundance ratios (van Dishoeck et al. 1996; van Dishoeck & Blake 1998), and the profiles of the ice bands, in particular solid CO₂ (Gerakines et al. 1999; Boogert et al. 2000). Thus, there is overwhelming evidence that thermal processing, i.e. evaporation and crystallization of ices in and around hot molecular cores, plays an important role in the evolution of high mass molecular envelopes.

The composition and evolution of the molecular material around low mass protostars are not as well studied. It seems unlikely that the molecular material evolves similar to that around high mass protostars. Low mass protostars evolve much slower, release less radiative energy, drive less energetic winds, and form disks. It is not established whether low mass objects possess hot cores as well, and whether the ices survive the process of star formation. If (some of) the ices survive, are they included into comets, and if so, are the ice structure and composition still the same compared to interstellar ices? How important are energetic processes, such as cosmic ray bombardment, in altering the ice composition on the long time scale of the formation of low mass stars?

To investigate the influence of low mass protostars on their molecular envelope, we make an infrared spectroscopic study Elias 29, also called WL 15 and YLW 7 (Elias 1978, Wilking et al. 1983, Young et al. 1986). On a large scale, Elias 29 lies in core E, which is in the south-east corner of the 1×2 pc extended compact CO ridge L 1688 (Loren et al. 1990) in the densest part of the ρ Ophiuchi cloud, at a distance of \sim 160 pc from the earth (Wilking & Lada 1983; Whittet 1974). It is the reddest object found in the near-infrared survey of this cloud by Elias (1978), without a counterpart at optical wavelengths. For our observations, we used Elias' coordinates (J2000):

$$\alpha = 16^{\text{h}}27^{\text{m}}09^{\text{s}}.3 \quad \delta = -24^{\circ}37'21''.$$

The overall spectrum of Elias 29 is typical for a heavily embedded Class I source, probably in a late accretion phase (Wilking et al. 1989; André & Montmerle 1994; Greene & Lada 1996; Saraceno et al. 1996). The embedded nature is also revealed by its high extinction, and by the cold compact envelope observed at millimeter wavelengths (André & Montmerle 1994; Motte et al. 1998). Elias 29 is associated with a molecular outflow (Bontemps et al. 1996; Sekimoto et al. 1997). With a bolometric luminosity of \sim 36 L_{\odot} (Chen et al. 1995), Elias 29 is the most luminous protostar in the ρ Oph cloud, which makes this source very suitable for spectroscopic studies. The relatively high luminosity, and high bolometric temperature ($T_{\text{bol}} \sim$ 410 K) imply an age in the range 0.5–4 10^5 yr

(Chen et al. 1995). In the pre-main-sequence evolutionary tracks of Palla & Stahler (1993), this corresponds to a star with end mass 3.0–3.5 M_{\odot} . Elias 29 might thus be a precursor Herbig AeBe star. This classification is however uncertain. For example, it has been argued from the SED, and the absence of mid-infrared emission features, that Elias 29 is a 1 M_{\odot} protostar with a large accretion luminosity, and a spectral type of K3-4 at the birth line (Greene & Lada 2000).

This Paper is structured as follows. Technical details on the ISO infrared observations are given in Sect. 2. All the observed emission and absorption features are discussed in detail in Sect. 3. Section 3.1 gives a description of the continuum shape, and a comparison to other lines of sight. The ice composition and thermal history, and the silicate band depth with inferred extinction and column densities toward Elias 29 are discussed in Sect. 3.2. Then, numerous lines of gaseous CO and H₂O are detected, and modeled to derive gas temperatures and column densities (Sect. 3.3). The molecular abundances and gas-to-solid ratios of Elias 29 are compared to a sample of sight-lines, ranging from dark cloud cores to evolved protostars. A comparison with high mass protostars is made (Sect. 4.1). Section 4.2 discusses the origin of the wealth of observed emission and absorption features and puts them in a geometrical picture, where we review the evidence for an extended envelope and an accretion disk. We conclude in Sect. 5 with a summary and suggestions for future observations.

2. Observations

2.1. The 2.3–45 μm spectrum

A low resolution ($R = \lambda/\Delta\lambda = 400$), full 2.3–45 μm spectrum of Elias 29 was obtained with the ISO *Short Wavelength Spectrometer* (ISO-SWS; de Graauw et al. 1996) during revolution 267 (August 10 1996). The ISO-SWS pipeline and calibration files, available in July 1998 at SRON Groningen, were applied. The spectrum is generally of good quality, with well-matching up and down scans, and no serious dark current problems, except for band 2C (7–12 μm). Here, we found that the up and down scans deviate over the silicate band. One scan showed good agreement with a ground-based spectrum of Hanner et al. (1995), and we used this to correct the deviating scan. Standard after-pipeline steps were applied, such as low order flat-fielding, sigma clipping and re-binning (see also Boogert et al. 1998). The twelve sub-spectra in the 2–45 μm range match fairly well at the overlap regions. Small correction factors (<15%) were applied to correct for the band jumps.

At selected wavelength ranges (3–3.6, 4–9, and 19.5–28 μm), we also obtained high resolution ($R = 1500$) ISO–SWS grating spectra, in revolution 292 (September 04 1996). These were reduced similarly to the low resolution spectrum. We found that the overall shape of the spectrum near 4–5 μm is quite badly affected by detector memory effects, presumably due to the occurrence of scan breaks (de Graauw et al. 1996). We corrected for this, by applying a wavelength-dependent shift to match the low resolution spectrum. This does not affect our conclusions, since the high resolution spectrum was only used to study narrow features. Also, near 6.9 μm the scans deviate significantly because of memory effects. This problem is reflected in the large error bars given in this paper, as they were derived from the difference between the average up and down scans.

2.2. The 45–190 μm spectrum

Elias 29 was observed during Revolution 484 (March 14 1997) with the *ISO Long Wavelength Spectrometer* (ISO–LWS; Clegg et al. 1996). We obtained 15 scans covering the range from 43 μm to 197 μm in the low resolution mode ($R \sim 200$) for a total of 2611 sec of integration time. The data were reduced using the Off-Line-Processing package (OLP) version 7 and the ISO–Spectral-Analysis-Package (ISAP) version 1.3. The spectra were flux calibrated using Uranus (Swinyard et al. 1996). We find that at the ISO–SWS/LWS overlap region near 45 μm , LWS has 35% higher flux than SWS. This difference is only slightly larger than the absolute calibration uncertainties of the two instruments, and thus it is doubtful that this can be ascribed to the presence of extended emission in the larger aperture of ISO–LWS ($\sim 80''$ versus $\sim 25''$). We therefore decided to multiply the LWS spectrum down with this factor.

3. Results

3.1. The spectral energy distribution (SED)

Elias 29 is only visible at wavelengths larger than $\sim 1.5 \mu\text{m}$ (Greene & Lada 1996; Elias 1978). Our ISO observations show that the continuum emission rises steeply between 2–3 μm , reaches a maximum of $\lambda F_\lambda = 15 \times 10^{-16} \text{ W cm}^{-2}$ at $\lambda \sim 5 \mu\text{m}$, and is remarkably flat with $\lambda F_\lambda \sim 8 \times 10^{-16} \text{ W cm}^{-2}$ between 20 and 100 μm (Fig. 1). The emission has dropped to $\lambda F_\lambda \sim 4 \times 10^{-16} \text{ W cm}^{-2}$ at 200 μm , and by four orders of magnitude at 1300 μm . Our near-infrared spectral continuum fluxes are in excellent agreement with broad band fluxes from ground-based observations (Elias 1978). Also the ground-based small beam

10 and 20 μm observations, as well as the large beam 12 and 25 μm IRAS fluxes, match the ISO–SWS observation well, thus indicating that at these wavelengths the emission is well confined within a region of $8''$ in diameter (Fig. 1; Lada & Wilking 1984; Young et al. 1986). The reasonable match of the ISO–SWS and LWS spectra (Sect. 2.2) indicates that also at 45 μm the emission is not very extended ($< 25''$). At 100 μm , however, some large scale emission may be present, since the IRAS flux, observed in a 5.5 times larger aperture, is a factor of 2 larger compared to the ISO measurement.

The observed SED of Elias 29 is different from that of massive protostars such as GL 2591, and GL 7009S, which peak in the far-infrared (Fig. 2). It has been proposed that the shape of SEDs is independent of the luminosity of the central object, and is rather determined by the total dust column density along the line of sight (Ivezic & Elitzur 1997). In the “standard model” of Ivezic & Elitzur, GL 2591 and GL 7009S would have a column density corresponding to an A_V of several hundred. Elias 29 must have an $A_V < 100$, because it does not peak in the far infrared. However, the flatness of the SED up to 100 μm is not reproduced in these models. A lower column density alone thus cannot explain the differences between the SED of Elias 29 and massive protostars. Other factors, such as a different density gradient, and the presence of a circumstellar disk are probably important. We will discuss the structure of Elias 29, in relation to the detected gas and ice absorption features, in Sect. 4.2.

3.2. Ice and dust absorption bands

Numerous absorption bands of ices and silicates are present in the infrared spectrum of Elias 29 (Fig. 3), such that hardly any ‘clean’ continuum emission is left. We identify each band, derive column densities, and, when possible, determine the ice mantle composition and thermal history. The full spectrum also allows a determination of upper limits of abundances for undetected, though astrophysically relevant molecules. The column densities for the species discussed below are summarized in Table 1.

3.2.1. H₂O ice

The infrared spectrum of Elias 29 shows all the vibration modes of H₂O ice in absorption (Fig. 4). We see the O–H stretching mode at 3.0 μm (“ ν_1, ν_3 ” in spectroscopic notation), the O–H bending mode at 6.0 μm (“ ν_2 ”), the libration or hindered rotation mode at $\sim 12 \mu\text{m}$ (“ ν_L ”), the combination mode at 4.5 μm (“ $3\nu_L$ ” or “ $\nu_2 + \nu_L$ ”), and perhaps the lattice mode at $\sim 45 \mu\text{m}$.

The continuum determination is complicated by the large width of all these bands. In accordance with other studies (Smith et al. 1989; Schutte et al. 1996; Keane et al. 2000), we used single blackbodies to fit the continuum

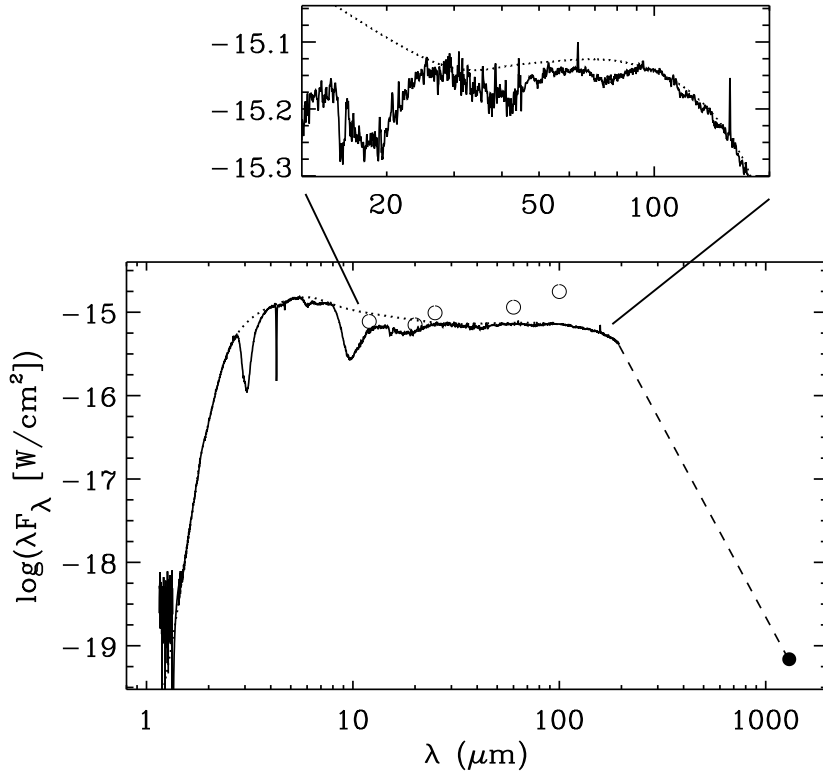


Fig. 1. Spectral energy distribution of Elias 29, consisting of ground-based observations ($\lambda < 2.4 \mu\text{m}$; Greene & Lada 1996), an ISO-SWS spectrum ($\lambda = 2.4\text{--}45 \mu\text{m}$), and an ISO-LWS spectrum ($\lambda = 45\text{--}195 \mu\text{m}$). The data point at $1300 \mu\text{m}$ is taken from André & Montmerle (1994), which we have connected with a dashed straight line to the ISO-LWS spectrum, to guide the eye. The dotted line is the adopted continuum, as determined by blackbody fits and by hand. The open circles are ground-based and IRAS observations (see text). The top inset shows a magnification of the $10\text{--}200 \mu\text{m}$ region.

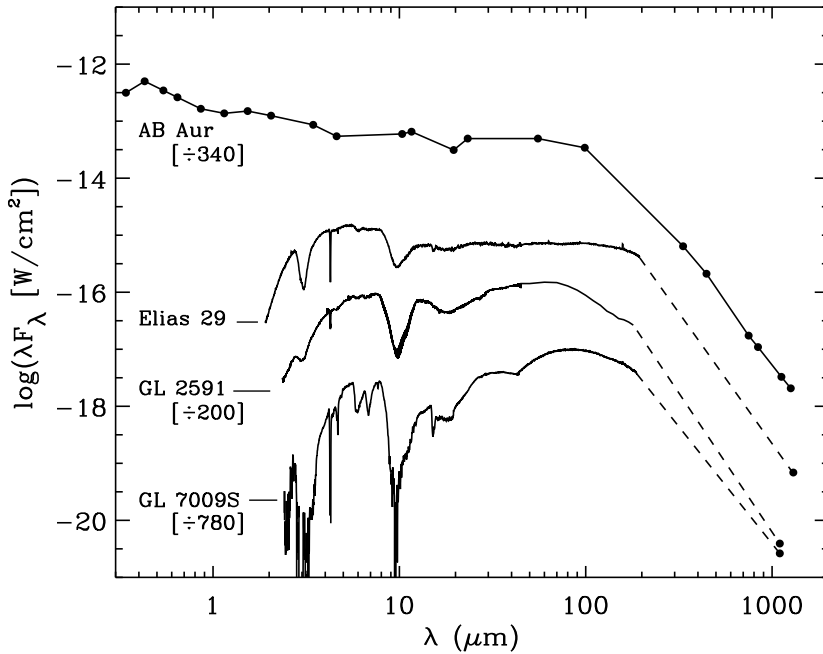


Fig. 2. Spectral energy distribution of Elias 29 compared to the high mass protostars GL 7009S (Dartois et al. 1998a), and GL 2591 (van der Tak et al. 1999). The spectrum of the Herbig Ae star AB Aur is a compilation of continuum observations taken from Mannings (1994), and is further discussed in Sect. 4.2. The flux scale of each spectrum has been divided by the values given in brackets.

locally, directly adjacent to the absorption bands. For the $6 \mu\text{m}$ band we took into account that laboratory spectra of the bending mode of H_2O ice show a prominent wing on the long wavelength side, extended up to $8 \mu\text{m}$ (e.g. Hudgins et al. 1993, Maldoni et al. 1998). We simultaneously fitted a blackbody continuum, normalized at $5.1 \mu\text{m}$, and

a laboratory ice spectrum to the observed flux at $8 \mu\text{m}$ and the shape of the $6.0 \mu\text{m}$ feature (Fig. 5).

The shape of the $6.0 \mu\text{m}$ H_2O bending mode is particularly sensitive to the ice temperature (e.g. Maldoni et al. 1998). At higher T in the laboratory, the strength of the main $6.0 \mu\text{m}$ component decreases at the expense of more absorption in the long wavelength wing. In the spectrum

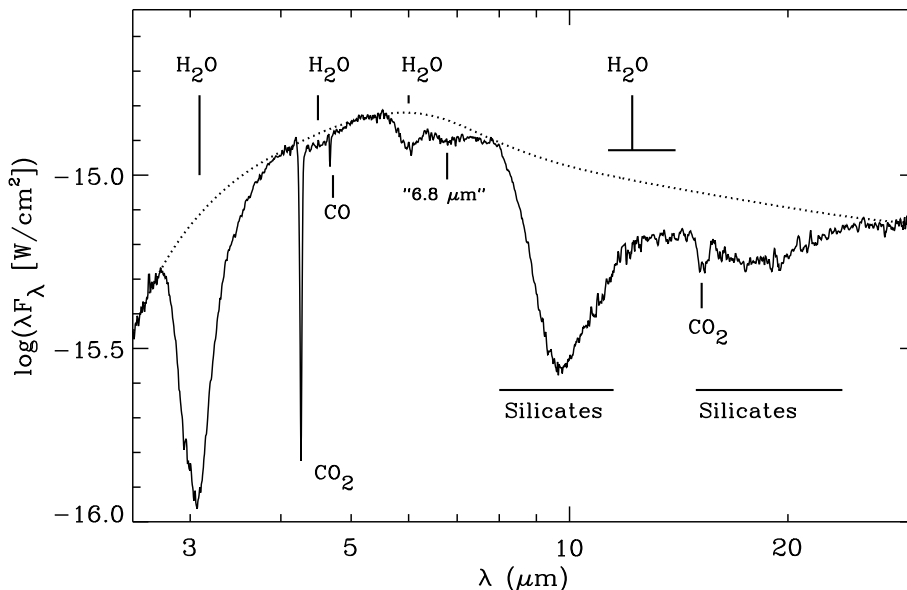


Fig. 3. Low resolution ($R = 400$) mid-infrared ISO-SWS spectrum of Elias 29 with a smooth, global continuum (dotted line), rather arbitrarily determined by hand and blackbody fits. The vibrational absorption bands of various molecules are indicated.

of Elias 29, the wing cannot be seen as a separate feature, since at $8 \mu\text{m}$ it blends with the very deep silicate band. However, the observed $6.0 \mu\text{m}$ band is relatively sharp, and it can only be fitted with H_2O ice at $T < 80 \text{ K}$, with a best fit at $T = 40 \text{ K}$ (Fig. 5). The excellent fit to the $6.0 \mu\text{m}$ band in Elias 29 indicates that the 5.83 and $6.2 \mu\text{m}$ excess absorptions detected toward several massive protostars (Schutte et al. 1996, 1998; Keane et al. 2000), are not seen in this source (Sect. 3.2.7).

The observed peak position of the stretching mode of H_2O ice toward Elias 29 is $3.07 \pm 0.01 \mu\text{m}$. The short wavelength wing is well matched with a laboratory ice at $T = 40 \text{ K}$, as for the bending mode (Fig. 5). The long wavelength wing, however, is poorly fitted. It has been realized since long that light scattering by large ice grains leads to

extra extinction on the long wavelength wing (e.g. Léger et al. 1983). To illustrate this, we calculate the extinction cross section for spherical silicate grains coated with ice mantles, applying the code given in Bohren & Huffman (1983) and the optical constants of Draine & Lee (1984) and Hudgins et al. (1993). Indeed, grains with a core+mantle radius of $\sim 0.6 \mu\text{m}$ provide a much better fit to the long wavelength wing than small grains do (Fig. 5). This effect is unimportant for the $6.0 \mu\text{m}$ band since it is intrinsically weaker, and the grains are smaller compared to the wavelength. In a more realistic approach, a distribution of grain sizes, as well as constraints to other observables such as continuum extinction, the total grain and ice column densities, and polarization need to be taken into account. Although there is a general consensus that large grains need to be invoked (e.g. Léger et al. 1983; Pendleton et al. 1990; Smith et al. 1989; Martin & Whitet 1990), there is no unified grain model yet that obeys all the observational constraints (e.g. Smith et al. 1993; Tielens 1982). Alternative absorbers at the long wavelength wing have been proposed, such as $\text{H}_2\text{O}.\text{NH}_3$ bondings. As illustrated in Fig. 5, this effect is however small at the low column density ratio of $\text{NH}_3/\text{H}_2\text{O} < 0.13$ toward Elias 29 (Sect. 3.2.7). A small contribution is also made by absorption by hydrocarbons (Sect. 3.2.4).

The peak optical depth of the $3.0 \mu\text{m}$ band is 1.85 ± 0.08 , which is in excellent agreement with the study of Tanaka et al. (1990). Using an integrated band strength $A = 2.0 \times 10^{-16} \text{ cm molecule}^{-1}$, we derive a column density of $N(\text{H}_2\text{O}) = 3.0 \times 10^{18} \text{ cm}^{-2}$ for the small grain model, and $3.7 \times 10^{18} \text{ cm}^{-2}$ for the large grain model. Since at present we can not favor one of these two cases, we

Table 1. Column densities of ices toward Elias 29. Non-detections are indicated with 3σ upper limits.

molecule	$N [10^{17} \text{ cm}^{-2}]$
H_2O	34 (6)
$^{12}\text{CO}_2$	6.7 (0.5)
$^{13}\text{CO}_2$	0.083 (0.005)
CO	1.7 (0.3)
CH_4	< 0.5
NH_3	< 3.5
CH_3OH	< 1.5
H_2CO	< 0.6
HCOOH	< 0.3
OCS	< 0.015
XCN	< 0.067

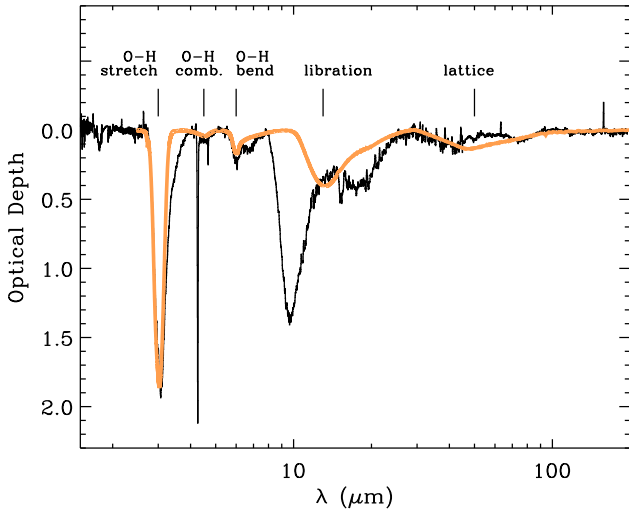


Fig. 4. Optical depth spectrum of Elias 29, assuming the continuum indicated in Figs. 1 and 3. The light, thick line is a laboratory spectrum of H_2O ice at $T = 10$ K (Hudgins et al. 1993). All five H_2O ice vibration bands can be discerned.

will assume an average value of $N(\text{H}_2\text{O}) = (3.4 \pm 0.6) \times 10^{18} \text{ cm}^{-2}$ in this paper. The error bar also includes the uncertainty in band strength, which increases with 10% when the ice is heated from 10 to 100 K (Gerakines et al. 1995). Note that a column density determination from the $6.0 \mu\text{m}$ bending mode is more uncertain due to the unreliable continuum on the long wavelength side (Fig. 5). At this column density of H_2O ice, the depth of the other vibrational modes is in good agreement with the observed spectrum of Elias 29 (Fig. 4).

3.2.2. CO ice

The CO ice band at $4.67 \mu\text{m}$ in Elias 29 is contaminated by gas phase CO lines from low J levels (Figs. 6 and 10). In particular, the P(1) line lies in the center of the ice band at $4.674 \mu\text{m}$. To study the band profile, we subtracted a model for the gaseous lines at $T_{\text{ex}} = 750$ K, $N = 5 \times 10^{18} \text{ cm}^{-2}$, and $b_{\text{D}} = 5 \text{ km s}^{-1}$ (Sect. 3.3). This increases the ice band width by 0.9 cm^{-1} , to $\text{FWHM} = 4.40 \text{ cm}^{-1}$ ($0.010 \mu\text{m}$). With a peak position of $4.673 \mu\text{m}$ (2140.1 cm^{-1}), the CO ice band observed toward Elias 29 is similar to that of the luminous protostar NGC 7538 : IRS9 (Fig. 6; Tielens et al. 1991; Chiar et al. 1998). The main, narrow component at $4.673 \mu\text{m}$ is attributed to pure solid CO, or CO embedded in an environment of apolar molecules. In particular, mixtures with O_2 , at an O_2/CO ratio as much as 5 (Elsila et al. 1997; Chiar et al. 1998) provide good fits. Mixtures of CO with CO_2 are generally too broad (Ehrenfreund et al. 1997). While the apolar, volatile component dominates the spectrum, both

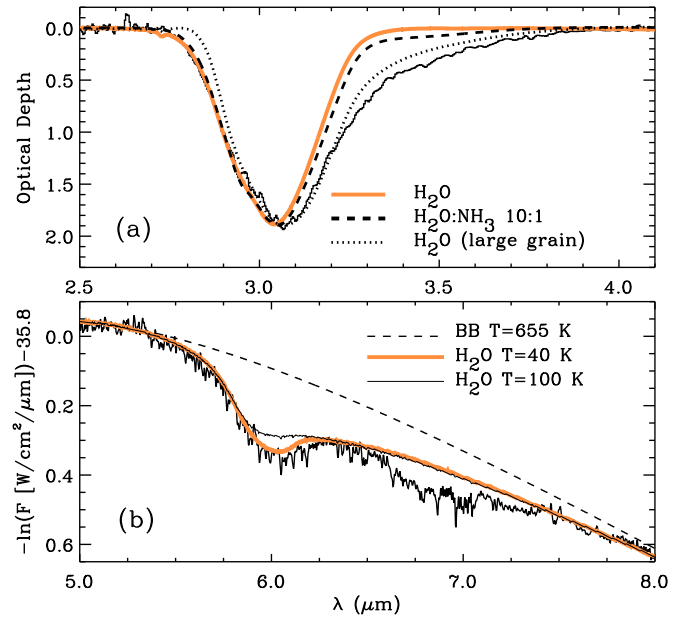


Fig. 5. Analysis of the $3.0 \mu\text{m}$ (a) and $6.0 \mu\text{m}$ (b) absorption bands of H_2O ice. In panel a, the thick gray line is a laboratory spectrum of pure H_2O ice at $T = 40$ K. The dashed line is a spectrum of $\text{H}_2\text{O}:\text{NH}_3 = 10:1$ ($T = 50$ K). The dotted line gives a calculated band profile of a large ice grain (see text). Panel b shows the $5\text{--}8 \mu\text{m}$ spectrum, with laboratory spectra at $T = 40$ K (thick gray line), and at $T = 100$ K (thin, solid line), showing that only low temperatures provide good fits to Elias 29. The dashed line shows the assumed blackbody continuum. The narrow absorption lines in the observed spectrum originate from H_2O vapor (Sect. 3.3).

Elias 29 and NGC 7538 : IRS9 show evidence for a wing on the long wavelength side. This is attributed to CO diluted in a mixture of polar molecules such as H_2O and CH_3OH (Chiar et al. 1998; Tielens et al. 1991). Assuming a band strength $A = 1.1 \times 10^{17} \text{ cm molecule}^{-1}$ for both the polar and apolar components (Gerakines et al. 1995), we derive $N(\text{CO ice}) = 1.7 \times 10^{17} \text{ cm}^{-2}$ with an apolar/polar ratio of ~ 8 , comparable to NGC 7538 : IRS9. These results are in good agreement with the ground-based study of Kerr et al. (1993). Although NGC 7538 : IRS9 seems to have a larger polar CO component in Fig. 6, this difference may merely reflect uncertainties in the continuum subtraction, and the fact that the NGC 7538 : IRS9 spectrum is not corrected for gas phase CO lines.

3.2.3. CO_2 ice

The absorption bands of CO_2 ice are prominently present in the infrared spectrum of Elias 29 (Fig. 3). We see the stretching and bending modes at 4.27 and $15.2 \mu\text{m}$ respectively. Not visible in this spectrum is the stretching mode

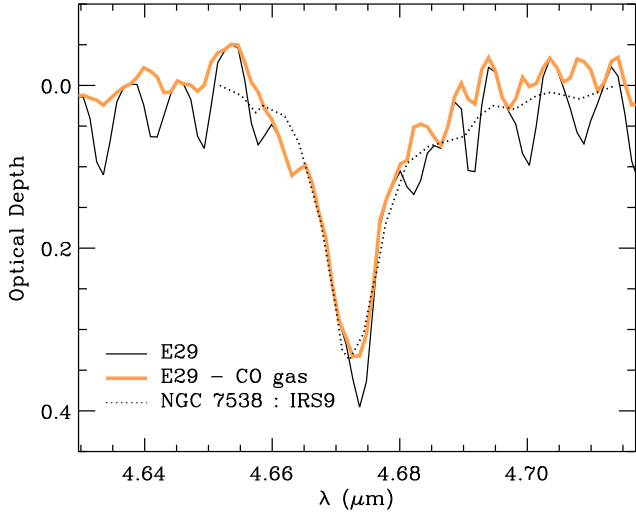


Fig. 6. The CO ice band on optical depth scale observed toward Elias 29 (thin solid line). The thick gray line is the spectrum with a gas phase CO model subtracted (see text). The dotted line represents the spectrum of the high mass protostar NGC 7538 : IRS9 (divided by 7.5; Tielens et al. 1991) showing the similarity of the band profiles.

of solid $^{13}\text{CO}_2$ at $4.38 \mu\text{m}$, although the high resolution spectrum (Fig. 10) shows a hint of its presence. A very sensitive observation is presented elsewhere (Boogert et al. 2000). The $^{12}\text{CO}_2$ bending mode and the $^{13}\text{CO}_2$ stretching mode have proven to be very sensitive to ice mantle composition and thermal history. In Elias 29, these bands do not show the narrow substructures seen in many other protostars, and attributed to heated polar CO_2 ices (Boogert et al. 2000; Gerakines et al. 1999). As for the CO ice band (Fig. 6), the width and peak position of the $^{13}\text{CO}_2$ band very much resemble that of the luminous protostar NGC 7538 : IRS9. Thus, the CO_2 ice toward Elias 29 is mixed in with polar molecules, and is not much affected by heating. The $^{12}\text{CO}_2$ column density is $22 \pm 4\%$ relative to H_2O ice, which is comparable to the values reported for high mass protostars (Gerakines et al. 1999). Finally, we derive an isotope ratio of $^{12}\text{CO}_2/^{13}\text{CO}_2 = 81 \pm 11$ in the ice toward Elias 29, which is well within the range found for the local ISM (Boogert et al. 2000).

3.2.4. The $3.47 \mu\text{m}$ band

The long wavelength wing of the deep $3.0 \mu\text{m}$ absorption band shows a change of slope at $3.38 \mu\text{m}$, indicative of a shallow absorption feature (Fig. 7). This feature is also detected in an independent ground based study of Elias 29 (Brooke et al. 1999). For consistency with ground based studies, the continuum on each side of the feature was assumed to start at 3.37 and $3.61 \mu\text{m}$. It must be emphasized however, that in particular on the long wavelength side,

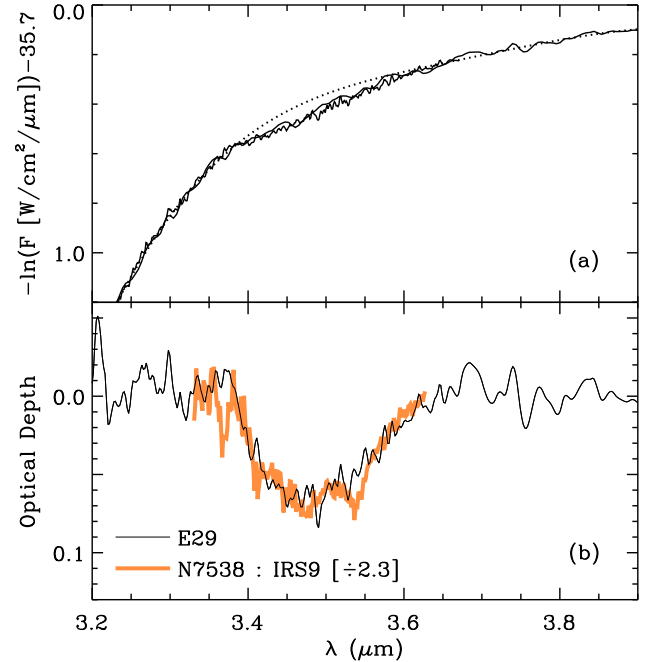


Fig. 7. a and b. Spectral structure in the long wavelength wing of the $3.0 \mu\text{m}$ band. **a** the merged high ($R = 1500$) and low ($R = 400$) resolution spectra and the assumed polynomial continuum (dotted line). **b** optical depth plot of the detected $3.47 \mu\text{m}$ feature. The gray, thick line represents the ground based spectrum of the high mass protostar NGC 7538 : IRS9, divided by a factor of 2.3 (Brooke et al. 1999), showing the C–H stretch mode of solid CH_3OH at $3.54 \mu\text{m}$. This feature is absent in the spectrum of Elias 29.

the continuum is poorly defined. Fitting a smooth 6-th order polynomial results in an absorption band centered on $3.49 \pm 0.03 \mu\text{m}$ with a peak optical depth of $\tau = 0.06$ (Fig. 7). The width is $\text{FWHM} = 120 \pm 40 \text{ cm}^{-1}$, where the uncertainty includes the poorly constrained continuum on the long wavelength side. Features of similar width and peak position have been detected in several massive protostellar objects (Allamandola et al. 1992) and in low mass objects and quiescent molecular cloud material (Chiar et al. 1996). A likely candidate for this $3.47 \mu\text{m}$ band is the C–H stretching mode of hydrocarbons. From the correlation of peak optical depths of this feature and the $3.0 \mu\text{m}$ ice band, it is concluded that the carrier for the $3.47 \mu\text{m}$ band resides in ices rather than in refractory dust (Brooke et al. 1996). We find that with $\tau(3.47 \mu\text{m}) = 0.06$ and $\tau(3.0 \mu\text{m}) = 1.85$, Elias 29 follows this correlation very well.

3.2.5. CH_3OH ice

In several high mass protostars, the $3.47 \mu\text{m}$ band is blended with a distinct narrow feature centered on

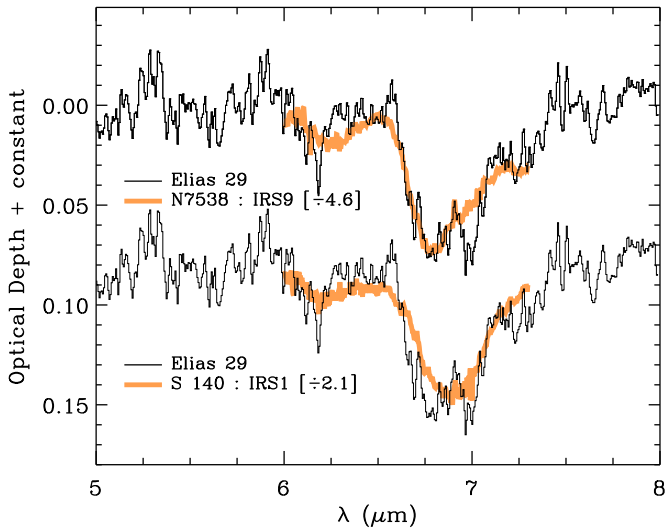


Fig. 8. Optical depth plot of the 5–8 μm region of Elias 29, after subtraction of an H_2O ice spectrum at $T = 40$ K as well as an H_2O gas model at $T_{\text{ex}} = 300$ K, $N = 2 \times 10^{18} \text{ cm}^{-2}$, $b_{\text{D}} = 2.5 \text{ km s}^{-1}$. This figure highlights the 6.85 μm absorption feature. The thick gray lines give a comparison with the massive protostars NGC 7538 : IRS9 (top) and S 140 : IRS1 (bottom; shifted down 0.08 along the optical depth axis).

3.54 μm (Allamandola et al. 1992). This feature is ascribed to the C–H stretching mode of solid CH_3OH . A direct comparison with the high mass protostar NGC 7538 : IRS9 shows that, although the 3.47 μm bands have similar shapes, the 3.54 μm feature is absent in Elias 29 (Fig. 7). We determine a 3σ upper limit to the peak optical depth of $\tau(3.54 \text{ } \mu\text{m}) < 0.036$. Scaling with the observed depth and column density in NGC 7538 : IRS9 (Brooke et al. 1999), then results in an upper limit to the CH_3OH ice column density $N(\text{CH}_3\text{OH ice}) < 1.5 \times 10^{17} \text{ cm}^{-2}$, or less than 5% of H_2O ice toward Elias 29 (Table 3). The other modes of CH_3OH ice are either much weaker, or are severely blended with the strong H_2O and silicate bands (e.g. the C–O stretching mode at 9.7 μm ; Schutte et al. 1991; Skinner et al. 1992) and thus do not provide better constraints on the CH_3OH ice column density. Toward other low mass objects, and quiescent dark clouds, low upper limits have been set to the CH_3OH ice abundance as well. The CH_3OH ice abundance found in massive protostars is generally of the same magnitude (Chiar et al. 1996), but in a few objects significantly larger (Dartois et al. 1999), than these upper limits.

3.2.6. The 6.85 μm band

Elias 29 is the first low mass protostar in which the 6.85 μm absorption band is detected (Fig. 5). After subtraction of the H_2O ice band and the gas phase H_2O lines

(Fig. 8), we find that it has a peak optical depth of $\tau \sim 0.07$ and an integrated optical depth $\tau_{\text{int}} = 7.8 \pm 1.6 \text{ cm}^{-1}$. When scaled to the H_2O ice column density, the strength of the 6.85 μm band toward Elias 29 is similar to high mass protostars (Keane et al. 2000). The band profile, e.g. the sharp edge at 6.60 μm , agrees very well with several high mass objects, in particular those tracing ‘cold’ gas and dust (NGC 7538 : IRS9, W 33A, GL 989). It clearly deviates from warmer lines of sight (e.g. S 140 : IRS1; Fig. 8). Thus, in this picture, we find that the material responsible for the 6.85 μm band toward Elias 29 is not significantly thermally processed. Given the low upper limits to the CH_3OH ice column density toward Elias 29, only a fraction of the band, as for high mass objects, can be explained by the C–H bending mode of CH_3OH ices (Schutte et al. 1996). For a detailed band profile analysis and a discussion on the origin of the 6.85 μm band, we refer to Keane et al. (2000).

3.2.7. Upper limits to solid CH_4 , NH_3 , H_2CO , HCOOH , OCS , and ‘XCN’

Several solid state species have been detected toward luminous protostars, but are absent toward Elias 29. The deformation mode of solid CH_4 was detected toward protostars, with a peak position at 1303 cm^{-1} (7.67 μm), and a width $\text{FWHM} = 11 \text{ cm}^{-1}$ (Boogert et al. 1996; Dartois et al. 1998b). For Elias 29 we can exclude this band to a peak optical depth of $\tau < 0.03$, corresponding to $N(\text{CH}_4)/N(\text{H}_2\text{O}) < 1.5\%$. This 3σ upper limit is comparable to the detection in NGC 7538 : IRS9 (Boogert et al. 1996).

Solid NH_3 was detected by its 9.10 μm inversion mode toward NGC 7538 : IRS9 (Lacy et al. 1998). Using the band strength determined in Kerkhof et al. (1999), the NH_3 column density is 13% of H_2O ice. Recent detections in other highly obscured lines of sight give similar (W 33A; Gibb et al. 2000), or a factor 2 larger NH_3 abundances (Galactic Center; Chiar et al. 2000). To find this band in the deep silicate feature of Elias 29 we take the same approach as Lacy et al., by fitting a local straight line continuum to the wavelength regions 8.52–8.69 and 9.20–9.55 μm . As a check, we perform the same procedure to the ISO–SWS spectrum of NGC 7538 : IRS9 (Fig. 9). We confirm the detection of Lacy et al., although the peak optical depth $\tau \sim 0.16$ is a factor 2 lower in our case. We ascribe this difference to the calibration uncertainties of ISO–SWS at this wavelength (Leech 2000). For Elias 29, a feature with $\tau \sim 0.06$ might be present. However, due to the poorly defined long wavelength side of the continuum (Fig. 9) and the ISO–SWS calibration uncertainties, we will assume a conservative upper limit to this band of $\tau < 0.1$. This corresponds to a column density of $N(\text{NH}_3) < 3.5 \times 10^{17} \text{ cm}^{-2}$, i.e. $N(\text{NH}_3)/N(\text{H}_2\text{O}) < 13\%$. Other vibrational bands of NH_3 do not provide better constraints. The equally strong N–H stretching mode at

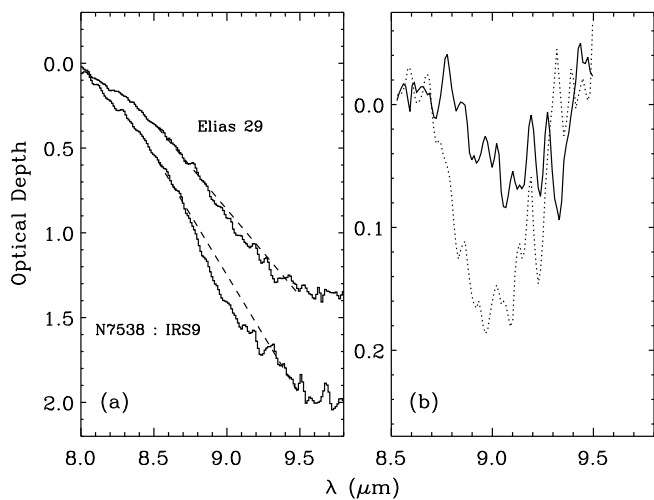


Fig. 9. **a** ISO-SWS spectra of the silicate band region of Elias 29 and NGC 7538 : IRS9. The dashed line is the local continuum for the solid NH_3 inversion mode, similar to that defined in Lacy et al. (1998). **b** the residuals after continuum subtraction for Elias 29 (solid) and NGC 7538 : IRS9 (dotted).

$2.90 \mu\text{m}$ (d’Hendecourt & Allamandola 1986) is hidden in the steep wing of the $3.0 \mu\text{m}$ ice band, and there is no significant difference in this region between the laboratory spectra of pure H_2O ice and the mixture $\text{H}_2\text{O}:\text{NH}_3=10:1$ (Fig. 5). A similar problem exists for the N-H deformation mode at $6.16 \mu\text{m}$, which is hidden in the long wavelength wing of the H_2O bending mode (Keane et al. 2000). A feature with a peak optical depth of $\tau < 0.025$ would be expected here (Sandford & Allamandola 1993). When subtracting water ice and vapor absorption, a weak band with an optical depth $\tau = 0.03$ perhaps remains present at the expected wavelength (Fig. 8). Given the other positive and negative structure in the spectrum, we regard this also as an upper limit, however.

The H_2O -subtracted $5.0\text{--}6.5 \mu\text{m}$ wavelength region (Fig. 8) does not show the features detected toward high mass protostars (Schutte et al. 1996; 1998; Keane et al. 2000). At $6.25 \mu\text{m}$ (not to confuse with the feature of NH_3 ice at slightly shorter wavelength; see above), a feature has been associated with absorption by carbonaceous dust (PAH). At $5.83 \mu\text{m}$ a broad feature has been assigned to the C=O stretching mode of solid HCOOH , and a narrow feature of solid H_2CO (Keane et al. 2000). Scaling the features observed toward NGC 7538 : IRS9 to the lower H_2O ice band column density toward Elias 29, one would expect peak optical depths $\tau_{5.83} = 0.06$ and $\tau_{6.25} = 0.03$. Our spectra indicate upper limits to these features of $\tau < 0.03$ (Fig. 8). Thus, in particular the $5.83 \mu\text{m}$ feature toward Elias 29 is significantly less pronounced compared to high mass protostars. Using the band strengths and typical widths given in Keane et al. (2000), we derive 3σ col-

umn density upper limits of $N(\text{H}_2\text{CO}) < 6 \times 10^{16} \text{ cm}^{-2}$, and $N(\text{HCOOH}) < 3 \times 10^{16} \text{ cm}^{-2}$. With abundance upper limits of 1–2% with respect to H_2O , these aldehydes are thus minor ice components. For comparison, toward high mass objects it is typically 3% or higher.

An absorption feature has been detected at $2042 \pm 4 \text{ cm}^{-1}$ ($4.90 \mu\text{m}$) in lines of sight toward several massive protostars (Palumbo et al. 1997). With a width $\text{FWHM} = 23 \pm 6 \text{ cm}^{-1}$, it has been ascribed to absorption by solid OCS. For Elias 29 this feature is not detected with a peak optical depth $\tau < 0.01$ (3σ), corresponding to $N(\text{OCS}) < 1.5 \times 10^{15} \text{ cm}^{-2}$ or $< 0.05\%$ of H_2O ice. This upper limit is of the same order of magnitude as the detections in W 33A and Mon R2 : IRS2 (Palumbo et al. 1997).

Finally, toward several high and low mass protostars a feature has been detected at $\sim 2166 \text{ cm}^{-1}$ ($4.62 \mu\text{m}$) with a width $\text{FWHM} \sim 20 \text{ cm}^{-1}$ (Lacy et al. 1984; Tegler et al. 1995). This feature is absent in Elias 29, with a peak optical depth $\tau < 0.01$ (3σ). If this feature is caused by the C \equiv N stretching mode in ‘XCN’, this corresponds to a column density $N(\text{XCN}) < 6.7 \times 10^{15} \text{ cm}^{-2}$, or less than 0.2% of H_2O ice (applying $A = 3 \times 10^{-17} \text{ cm molecule}^{-1}$; Tegler et al. 1995). This is considerably less than the detections made toward high mass objects (e.g. W 33A) and several low mass objects (Elias 18; L 1551 : IRS5; Tegler et al. 1995). This feature has not been detected in the quiescent regions of the Taurus molecular cloud (Elias 16; Table 3). For a more elaborate discussion on this feature, and the proposed carriers, we refer to Pendleton et al. (1999).

3.2.8. Silicates

The absorption bands of the Si-O stretching and bending modes of silicate dust are prominently present at $9.7 \mu\text{m}$ and $18 \mu\text{m}$ (Fig. 3). We derive a peak absorption optical depth of the $9.7 \mu\text{m}$ band $\tau_{9.7} = 1.38$ (Fig. 4), which is in excellent agreement with the ground-based study of Hanner et al. (1995). It is likely that this is a lower limit, since the absorption bands have been partly filled in with silicate emission from hot dust near the protostar. Modeling of the $9.7 \mu\text{m}$ silicate band toward Elias 29, including emission and absorption, shows that $\tau_{9.7}$ ranges between 1.51 and 3.38 for optically thick and thin emission respectively (Hanner et al. 1995). A better fit is obtained for optically thick emission. In contrast, for luminous protostars optically thin emission has been generally assumed. Using the relation $\tau_{9.7} = 1.4 \tau_{9.7}(\text{obs}) + 1.6$ (Gillet et al. 1975; Willner et al. 1982), yields $\tau_{9.7} = 3.53$ for Elias 29.

For these values of $\tau_{9.7}$, the visual extinction A_V ranges between 28 and 65, assuming the standard relation $A_V/\tau_{9.7} = 18.5$ (Roche & Aitken 1984). However, these limits are likely overestimated (30–50%), because of the anomalous extinction curve due to larger grains in the ρ Oph molecular cloud (Bohlin et al. 1978; Martin & Whitet 1990). Independent extinction determinations, such as

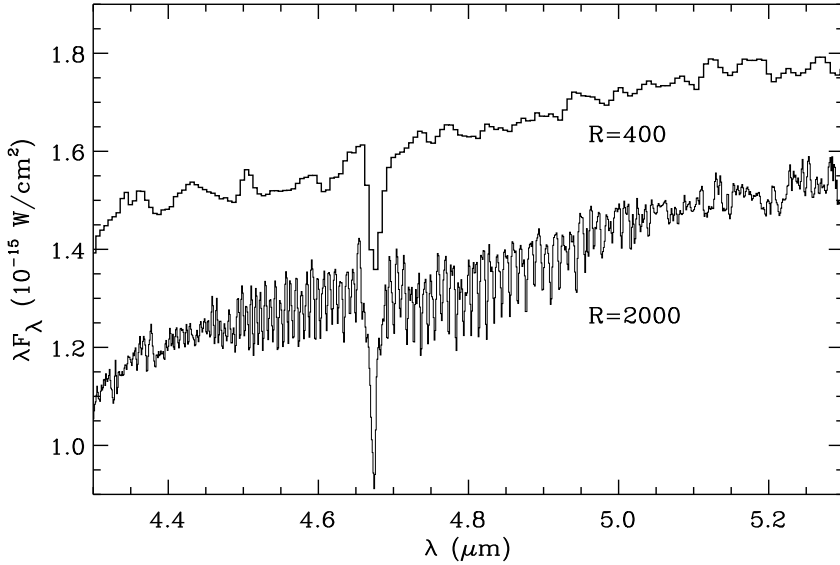


Fig. 10. High resolution ($R=2000$) spectrum of Elias 29 showing many gas phase CO lines, and the CO ice band at $4.67 \mu\text{m}$. The narrow emission line at $4.653 \mu\text{m}$ is Pf β of H I. Some of the narrow structure seen on the long wavelength side is due to lines of hot H_2O vapor (see text). For comparison we show a low resolution ($R=400$) observation, shifted along the flux scale for clarity, where the gas lines are smeared out over the continuum.

$A_V < 48$ from the H-K broad band color and $A_V < 80$ from C^{18}O observations (Wilking & Lada 1983), do not help to solve this issue. Millimeter continuum observations (André & Montmerle 1994), and the near-infrared J-H color (Greene, priv. comm.), suggest a relatively low $A_V < 30$.

The total hydrogen column density $N_{\text{H}} = N(\text{H I}) + 2N(\text{H}_2)$ is closely related to $\tau_{9.7}$, and, in contrast to the derivation of A_V , the derived N_{H} is not strongly affected by the large grain size in ρ Oph. Applying standard conversion factors for the diffuse ISM (Bohlin et al. 1978; Roche & Aitken 1984), we find $N_{\text{H}} = 0.5 - 1.2 \times 10^{23} \text{ cm}^{-2}$, depending on the applied $\tau_{9.7}$. To be consistent with studies of high mass protostars, we will assume in the abundance calculations, the value corresponding to optically thin silicate emission, i.e. the high limit $N_{\text{H}} = 1.2 \times 10^{23} \text{ cm}^{-2}$ (Table 3).

3.3. Gas phase absorption lines

The high resolution $4.00\text{--}8.50 \mu\text{m}$ spectrum of Elias 29 shows an impressive number of narrow absorption lines of gaseous CO and H_2O (Figs. 5 and 10). We determined local continuum points by hand and connected these, using a smooth cubic spline interpolation. Then the data were converted to optical depth scale, and the absorption lines were modeled, using the ro-vibrational spectra of gaseous CO and H_2O described in Helmich (1996). These models assume the gas is in Local Thermodynamic Equilibrium (LTE), and has a single excitation temperature T_{ex} . The absorption lines have a Voigt profile, and are Doppler broadened to a width b_{D} ($=\text{FWHM}/2\sqrt{\ln 2}$). The line oscillator strengths are calculated from the HITRAN database (Rothman et al. 1992). Finally, the spectrum is convolved with a Gaussian to the resolution of our obser-

ations ($R = 1500 - 2000$). Thus, three parameters are varied to fit the observed absorption lines: the column density N , the Doppler parameter b_{D} , and the excitation temperature T_{ex} . Reliable column densities can only be derived if b_{D} is a priori known, which in many studies (like ours) is not the case, since the lines are unresolved. At low values of b_{D} , the lines become easily optically thick, and much larger column densities are needed to fit the observed lines, compared to models with high b_{D} values, and optically thin lines.

We emphasize that our assumptions of collisional excitation, and LTE at a single T_{ex} need not be valid. There is likely a temperature gradient along the line of sight, as expected for a protostellar envelope. The LTE assumption may not apply for the high rotational levels, which have high critical densities. Also, the energy levels may be pumped by infrared photons, rather than being collisionally excited. Bearing these caveats in mind, we will here focus on deriving CO and H_2O gas column densities and temperatures using the LTE models.

3.3.1. CO gas

The $4.4\text{--}5.0 \mu\text{m}$ region shows absorption lines of gas phase ^{12}CO , up to rotational quantum number $J_{\text{low}}=33$ in the R-branch, and $J_{\text{low}}=36$ in the P-branch (Fig. 10). The P(1), P(2) and R(0) lines are blended with the CO ice band at $4.67 \mu\text{m}$ and the H I Pf β emission line at $4.653 \mu\text{m}$. For all other absorption lines we determined equivalent widths to construct a rotation diagram. A rotation diagram gives a first impression of the temperature components present along the line of sight, as well as their column densities (or lower limits for optically thick lines). For technical details on constructing such a diagram we refer to Mitchell et al. (1990), and Boogert et al. (1998). The equivalent widths were converted to column densities, using the oscillator

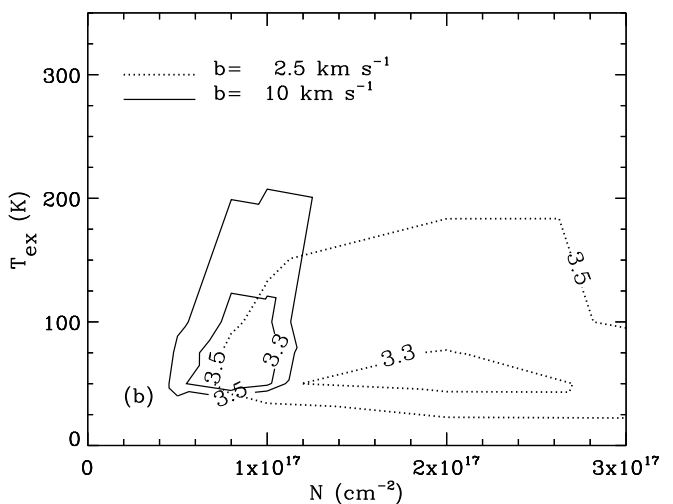
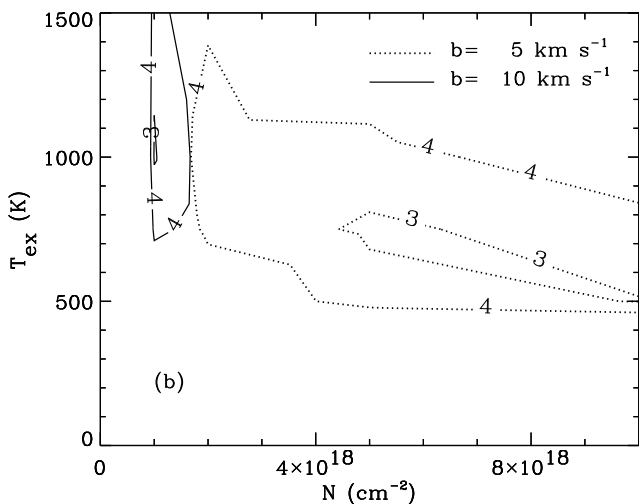
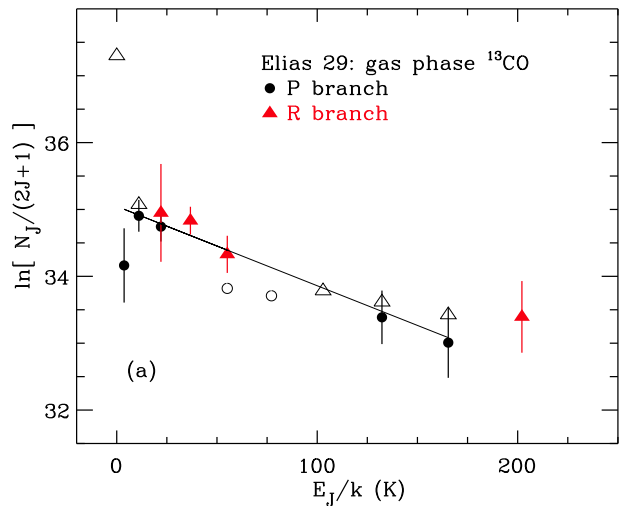
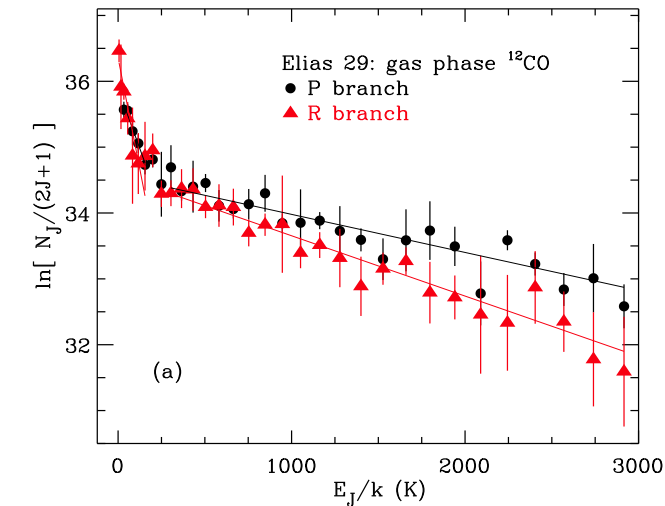


Fig. 11. **a** rotation diagram of the ^{12}CO lines detected toward Elias 29 showing the presence of hot and cold gas along the line of sight by the different slopes at high and low rotational levels. **b** χ^2_ν contour diagram of model fits to the observed ro-vibrational spectrum of the R-branch of gaseous CO toward Elias 29. χ^2_ν values are shown for the temperature T_{ex} versus CO column density N at constant velocity broadenings b_D of 5 km s^{-1} (dotted) and 10 km s^{-1} (solid). We only show models that provide acceptable fits to the data, i.e. $\chi^2_\nu < 4$.

Fig. 12. **a** Rotation diagram of the ^{13}CO lines detected toward Elias 29. Circles are P-branch lines, and triangles are R-branch lines. Open symbols refer to ^{13}CO lines heavily blended with ^{12}CO lines, and are not used to determine the physical parameters. The straight line indicates the best fit, with a gas temperature $T_{\text{rot}} = 85 \pm 57 \text{ K}$, and a column density $N(^{13}\text{CO}) = (1.1 \pm 0.2) \times 10^{17} \text{ cm}^{-2}$. **b** χ^2_ν contour diagram of model fits to the observed ro-vibrational spectrum of gaseous ^{13}CO toward Elias 29. χ^2_ν values are shown for the temperature T_{ex} versus CO column density N for constant velocity broadenings $b_D = 2.5 \text{ km s}^{-1}$ and $b_D = 10 \text{ km s}^{-1}$. Only acceptable fits to the data, having $\chi^2_\nu < 3.5$, are shown.

strengths of Goorvitch (1994). For ^{12}CO (Fig. 11), we find two regimes with very different slopes, corresponding to temperatures $T_{\text{rot}} = 90 \pm 45 \text{ K}$ and $T_{\text{rot}} = 1100 \pm 300 \text{ K}$ respectively (with 3σ errors). However, the slopes of the R- and P-branch lines of the hot component are different (Fig. 11), resulting in $T_{\text{rot}} = 1700 \pm 420 \text{ K}$ when fitting to the P-branch lines only. A possible explanation is that CO is excited by continuum photons rather than collisions. The rising continuum may lead to a higher T_{rot} for the P-branch with respect to the R-branch. This effect becomes

stronger when the photons released after de-excitation of R-branch levels are re-absorbed in P-branch levels. Radiative excitation has also been used to explain the H_2O ro-vibrational spectrum toward Orion BN/KL (Gonzalez-Alfonso et al. 1998). The fact that the H_2O P-branch lines are seen in emission for Orion BN/KL, rather than in absorption as for CO (and H_2O ; Sect. 3.3.2) toward Elias 29,

may reflect a different density gradient toward Elias 29, such that the photons are not able to escape the envelope. Additionally, collisional excitation in shocks may be of less importance in Elias 29 compared to Orion BN/KL. A more careful analysis is needed to discriminate between the radiative and collisional excitation models, and alternative explanations, such as non-LTE effects.

The column densities that we derive from the abscissa in the rotation diagram are $N(\text{CO})=1.7 \times 10^{17}$ and $N(\text{CO})=3.5 \times 10^{17} \text{ cm}^{-2}$ for the cold and hot CO components respectively. To better constrain the column densities and derive more reliable temperatures, one has to take into account optical depth effects, using the LTE model spectra discussed above. We chose to fit to the frequency range 2170–2290 cm^{-1} ($J_{\text{low}} > 7$ in R-branch), thus minimizing the contribution from the cold CO component and contamination by ^{13}CO lines (see below). We find that good fits to these high R-branch lines are obtained only for line widths $b_D > 3 \text{ km s}^{-1}$. Sub-millimeter emission line studies indicate $b_D=3.6 \text{ km s}^{-1}$ for CO $J=6 \rightarrow 5$, but much lower values of $b_D=1.2 \text{ km s}^{-1}$ for $\text{C}^{18}\text{O } J=1 \rightarrow 0$ and CS $J=5 \rightarrow 4$ (Boogert, Hogerheijde, et al., in prep.). Indeed, studies of other sources have shown that, as a rule, infrared absorption lines are broader than sub-millimeter emission lines (van der Tak et al. 1999). Figure 11 shows the χ_ν^2 contour diagram of temperature versus column density for two values of the line width $b_D=5$, and $b_D=10 \text{ km s}^{-1}$. The best fitting models have temperatures $T_{\text{ex}} = 1100 \pm 400 \text{ K}$, in good agreement with the rotation diagram. At $b_D=10 \text{ km s}^{-1}$ the column density is well constrained to $N(\text{CO})=(1.3 \pm 0.5) \times 10^{18} \text{ cm}^{-2}$, which is a factor of 3 larger compared to that derived from the rotation diagram. Thus at $b_D=10 \text{ km s}^{-1}$ the lines are still somewhat optically thick. At lower $b_D=5 \text{ km s}^{-1}$, the lines become very optically thick, and the column density is poorly constrained. Although the best fits with $\chi_\nu^2 < 3$ have $N(\text{CO})=(8 \pm 4) \times 10^{18} \text{ cm}^{-2}$ at $T_{\text{ex}} = 650 \pm 150 \text{ K}$, reasonable fits are obtained at any $N(\text{CO}) > 2 \times 10^{18} \text{ cm}^{-2}$ for this hot CO gas.

Several ^{13}CO lines can be seen in between the ^{12}CO P-branch lines (Fig. 13). At the resolution of our observations, the blending with the ^{12}CO lines hinders analyzing the much weaker ^{13}CO lines. But using several well separated lines, we were able to construct a rotation diagram (Fig. 12). We find that they result from cold gas at $T_{\text{rot}} = 85 \pm 57 \text{ K}$ (3σ error), in good agreement with the cold ^{12}CO gas temperature. In the optical thin case, the column density of this cold component is $N(^{13}\text{CO})=(1.1 \pm 0.2) \times 10^{17} \text{ cm}^{-2}$. However, the detected ^{13}CO lines could still be optically thick. Therefore, we also modeled the ^{13}CO spectrum, and determine the χ_ν^2 after subtraction of a good fitting hot ^{12}CO gas model (Figs. 13 and 12). In the optically thick case, such as for $b_D=2.5 \text{ km s}^{-1}$, the column density can have a wide range $N(^{13}\text{CO})=(2 \pm 1.3) \times 10^{17} \text{ cm}^{-2}$. Using the isotope abundance ratio $^{12}\text{CO}/^{13}\text{CO}=80$ (Boogert et al. 2000), the inferred cold ^{12}CO column den-

Table 2. Gas phase ^{12}CO and H_2O column densities, derived with various methods

Molecule	Method	$N [10^{18} \text{ cm}^{-2}]$	
		cold	hot
^{12}CO	rotation diagram	0.17	0.35
^{12}CO	LTE, $b_D=10 \text{ km s}^{-1}$	–	1.3 ± 0.5
^{12}CO	LTE, $b_D=5 \text{ km s}^{-1}$	–	> 2
^{13}CO	rotation diagram	9 ± 2^a	–
^{13}CO	LTE, $b_D=2.5 \text{ km s}^{-1}$	16 ± 10^a	–
H_2O	LTE ^b , $b_D=5 \text{ km s}^{-1}$	–	0.7 ± 0.4
H_2O	LTE ^b , $b_D=2.5 \text{ km s}^{-1}$	–	2.4 ± 2.1
H_2O	LTE ^c , $b_D=5 \text{ km s}^{-1}$	< 1	0.5
H_2O	LTE ^c , $b_D=2.5 \text{ km s}^{-1}$	< 10	0.5

^aConverted to $N(^{12}\text{CO})$ assuming $N(^{12}\text{CO})/N(^{13}\text{CO}) = 80$ (Boogert et al. 2000)

^bSingle temperature model with $T_{\text{ex}}=300 \text{ K}$

^cDouble temperature model with fixed $N_{\text{hot}} = 5 \times 10^{17} \text{ cm}^{-2}$

sity is thus $N(^{12}\text{CO})=(16 \pm 10) \times 10^{18} \text{ cm}^{-2}$. There is also evidence for ^{13}CO lines of warm gas ($J_{\text{low}} > 9$), but at low significance ($\leq 2\sigma$) and no reliable temperature or column density could be derived.

We conclude that the CO gas along the line of sight consists of two temperature components, $T_{\text{rot}} = 90 \pm 45 \text{ K}$ and $T_{\text{rot}} = 1100 \pm 300 \text{ K}$. The column density of both components depends highly on the assumed line optical thickness (Table 2). Until the intrinsic line width is directly observed by very high spectral resolution observations, we can only give a lower limit of $N(\text{CO-hot}) > 2 \times 10^{18} \text{ cm}^{-2}$, while $N(\text{CO-cold})$ is not well constrained, i.e. $(16 \pm 10) \times 10^{18} \text{ cm}^{-2}$. Given that $N_{\text{H}} = 1.2 \times 10^{23} \text{ cm}^{-2}$ toward Elias 29, a total gas phase CO column density $N(\text{CO})=12 \times 10^{18} \text{ cm}^{-2}$ is expected, assuming that most of the gas along the line of sight is molecular and the conversion factor $N(\text{H}_2)/N(\text{CO})=5000$ applies (Lacy et al. 1994). Then, the ratio of hot to cold CO gas along the line of sight must be at least 0.2.

3.3.2. H_2O gas

We compare the numerous narrow absorption lines detected in the 5–7.3 μm spectral region of Elias 29 with model spectra of H_2O vapor at various physical conditions (Fig. 14). Clearly, the many lines observed at wavelengths longer than $\sim 6.55 \mu\text{m}$ are explained by H_2O vapor at a high temperature ($T_{\text{ex}} > 100 \text{ K}$). On the other hand, the relative weakness of the lines observed in the range 6.55–6.65 μm imposes a strict upper limit to the temperature of this hot gas ($T_{\text{ex}} < 1000 \text{ K}$). To further constrain the gas temperature, and the H_2O vapor column density, we determined the χ_ν^2 for a large number of models. Reasonable fits to the full 5–7.3 μm range are obtained for

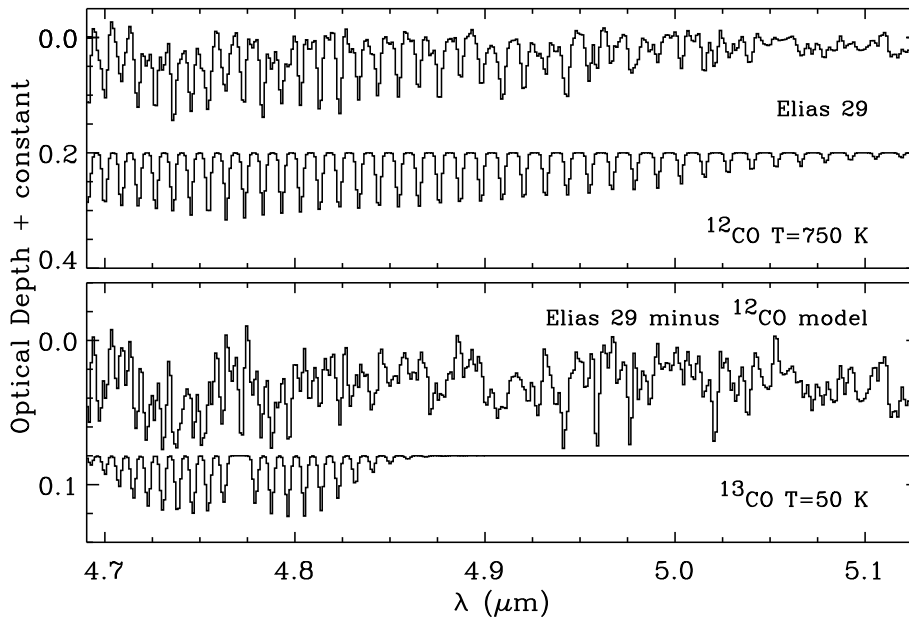


Fig. 13. The P branch of gas phase CO observed in Elias 29 (top) compared with a well fitting ^{12}CO gas model at $T_{\text{ex}} = 750$ K ($N = 5 \times 10^{18} \text{ cm}^{-2}$, $b = 5 \text{ km s}^{-1}$). The bottom panel shows the residual after subtraction of the ^{12}CO gas model, which contains lines of cold ^{13}CO gas. For comparison, a ^{13}CO model is plotted ($T_{\text{ex}} = 50$ K, $N = 2 \times 10^{17} \text{ cm}^{-2}$, $b = 2.5 \text{ km s}^{-1}$).

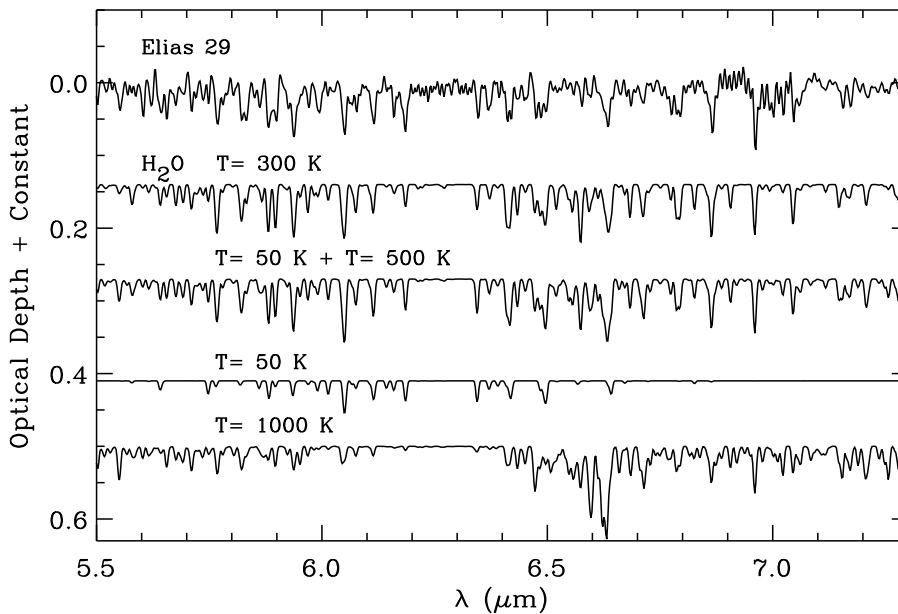


Fig. 14. Optical depth plot of gaseous H_2O lines observed toward Elias 29 (top), compared with model spectra at various temperatures. Column densities are $N = 5 \times 10^{17} \text{ cm}^{-2}$ for all models, and $b_{\text{D}} = 5.0 \text{ km s}^{-1}$ ($T_{\text{ex}} = 50$ K models have $b_{\text{D}} = 2.5 \text{ km s}^{-1}$). The single component $T = 300$ K and the two component $T = 50 + 500$ K models give equally good fits. The models with just cold ($T = 50$ K) or very hot ($T = 1000$ K) gas clearly do not fit the data.

temperatures of $T_{\text{ex}} = 350 \pm 200$ K. The column density is constrained to $N = (7 \pm 4) \times 10^{17} \text{ cm}^{-2}$ for low line optical

depths ($b_{\text{D}} \geq 5$). For narrower lines the column density can be an order of magnitude larger.

Table 3. Line-of-sight averaged solid and gas phase abundances (N/N_{H} in units of 10^{-6})

species	Dense Cloud ^a	N7538/9	W 33A	Elias 29	GL 2591	Refs. ^b
H ₂ O–ice	64	50	39-143	28 (8)	10	[1],[2],[3,4],[5],[6]
–gas ^c	<1	< 3.1	<3.6	>3	24 (3)	[7],[8],[8],[5],[8]
CO–ice ^d [total]	17 (1)	8 (1)	3.2 (1.8)	1.4 (0.2)	<< 1	[9],[9],[9],[5],[10]
–ice [apolar]	14 (1)	7 (0.5)	0.8 (0.1)	1.2 (0.2)	<< 1	[9],[9],[9],[5],[10]
–gas	< 10	91 (51)	143 (32)	> 67 ^b	113 (15)	[11],[12],[12],[5],[12]
CO ₂ –ice	12 (3)	10 (1)	5.2 (0.5)	5.4 (0.5)	0.9 (0.1)	[13],[13],[13],[13],[13]
–gas	–	0.05 (0.01)	0.08 (0.02)	<0.06	0.15 (0.03)	[8],[8],[8],[8]
NH ₃ –ice	–	7.6	6.1	< 3.0	–	[14],[3],[5]
CH ₃ OH–ice	< 1.8	2.0	7	< 1.3	4 (2)	[15],[15],[15],[5],[16]
H ₂ CO–ice	–	1.9	2.5	< 0.5	–	[4],[4],[5]
HCOOH–ice	–	1.1	0.6	< 0.3	–	[4],[4],[5]
CH ₄ –ice	–	0.8	0.6	< 0.4	–	[17],[17],[5]
OCS–ice	< 0.13	–	0.07	< 0.02	–	[18],[18],[5]
‘XCN’–ice	< 1.3	1 (0.3)	3.6 (1)	< 0.06	–	[19],[19],[19],[5]
N_{H} [10^{23} cm ⁻²] ^e	0.39	1.6	2.8	1.2	1.7	[20],[20],[20],[5],[21]

^a Ice abundances are for Taurus dense cloud toward Elias 16. Gas phase abundances are for ρ Oph cloud.

^b References from left to right for each column: [1] Chiar et al. 1995; [2] Schutte et al. 1996; [3] Gibb et al. 2000; [4] Keane et al. 2000; [5] this work; [6] Smith et al. 1989; [7] Liseau & Olofsson 1999; [8] Boonman et al. 2000; [9] Chiar et al. 1998; [10] van Dishoeck et al. 1996; [11] Caux et al. 1999; [12] Mitchell et al. 1990; [13] Gerakines et al. 1999; [14] Lacy et al. 1998; [15] Chiar et al. 1996; [16] Schutte et al. 1991; [17] Boogert et al. 1998; [18] Palumbo et al. 1997; [19] Tegler et al. 1995; [20] Tielens et al. 1991; [21] this work, Fig. 2

^c All models assume $b_{\text{D}}=5$ km s⁻¹ for hot gas and $b_{\text{D}}=2.5$ km s⁻¹ for cold gas

^d Total CO ice abundance given as well as the abundance present in the polar and apolar ice components along the line of sight

^e Determined from the 9.7 μm silicate band

In a second approach, we test whether both hot and cold H₂O vapor components could be present along the line of sight, much like the hot and cold CO components. We fitted the regions 5.5–5.8 and 6.55–7.3 μm , which do not contain lines from the lowest rotational levels and thus are particularly sensitive to warm H₂O vapor along the line of sight (Helmich et al. 1996; Dartois et al. 1998b). The excitation temperature of this gas is $T_{\text{ex}} = 500 \pm 300$ K, with column densities similar to that of the single component model. In the high temperature regime ($T_{\text{ex}} \geq 500$ K), the modeled line depths in the 6.0–6.5 μm region, tracing colder gas, are significantly underestimated. To determine the temperature and column density of this possible cold component, we fitted the sum of a good fitting hot gas model ($T_{\text{ex}} = 500$ K, $N = 5 \times 10^{17}$ cm⁻², $b_{\text{D}}=5.0$ km s⁻¹) and a grid of models at a wide range of physical conditions to the spectrum of Elias 29. Thus, here we assume that the lines of the hot and cold gas have different radial velocities and the optical depth spectra can simply be added. We find that indeed a significant amount of ‘cold’ H₂O vapor, at $T_{\text{ex}} < 200$ K may be present (Fig. 14). At $T_{\text{ex}} < 100$ K the column density exceeds the assumed hot H₂O column density of $N = 5 \times 10^{17}$ cm⁻². For a line width of $b_{\text{D}}=5.0$ km s⁻¹, we

find that $N < 1 \times 10^{18}$ cm⁻². At $b_{\text{D}}=2.5$ km s⁻¹, the column density of this cold H₂O gas cannot be constrained.

To summarize, the lines in the 5–7.3 μm range are reasonably fitted with H₂O models at $T_{\text{ex}} \sim 350 \pm 200$ K, and $N=(7 \pm 4) \times 10^{17}$ cm⁻² at low line optical depths. For narrower lines ($b_{\text{D}} < 5$ km s⁻¹), the column density can be an order of magnitude larger. In accordance with the gaseous CO along the line of sight, equally good fits are obtained with a two component model, where the cool component has $T_{\text{ex}} < 200$ K, and the warmer component $T_{\text{ex}} > 500$ K. The cool component is then at least as abundant as the warm H₂O gas.

4. Discussion

4.1. Gas and solid state abundances

We have calculated line of sight averaged gas and solid state abundances toward Elias 29, by dividing the column densities derived in this paper over the total hydro-

gen column density $N_{\text{H}} = 1.2 \times 10^{23} \text{ cm}^{-2}$ (Sect. 3.2)¹. We compare these abundances with a sample of sight-lines, spanning the range from dark cloud core to fairly evolved protostars (Table 3). As a tracer of ices in quiescent dark cloud material, we chose the object Elias 16, an evolved star by chance located behind the Taurus molecular cloud (e.g. Whittet et al. 1998). Gas phase CO and H₂O abundances in dense clouds were taken from ISO-LWS studies (Caux et al. 1999; Liseau & Olofsson 1999). The least evolved protostar in our comparison sample is NGC 7538 : IRS9. The infrared spectrum of this deeply embedded object is characterized by cold ice (Whittet et al. 1996), and the gas phase temperatures and abundances indicate a very modest hot core (Mitchell et al. 1990; Boonman et al. 2000). W 33A is more embedded than NGC 7538 : IRS9, but does have a significant amount of warm gas along the line of sight (Mitchell et al. 1990; Lahuis & van Dishoeck 2000; Boonman et al. 2000), and has a lower abundance of volatile ices (Tielens et al. 1991). The most evolved object in our sample is GL 2591. It is a typical high mass hot core source, with low ice abundances and high gas temperatures. All these protostars are associated with infrared reflection nebulae, and have well developed high velocity molecular outflows (Mitchell et al. 1991; Bontemps et al. 1996; van der Tak et al. 2000). Finally, it is important to note that all the comparison protostars are at least three orders of magnitude more luminous than Elias 29. This allows an investigation of the effect of low and high mass star formation on the molecular envelopes. An extensive comparison with low luminosity embedded objects is at present not possible, because their infrared gas and solid state characteristics have not been studied in such great detail.

The H₂O and CO ice abundances decrease for the sequence of quiescent dense cloud to NGC 7538 : IRS9, W 33A and GL 2591 (Table 3). At the same time, the gas phase H₂O abundance, the gas phase CO and H₂O temperatures, as well as the gas-to-solid ratios (Table 4), increase for these objects. All these effects can be explained by evaporation of the ice mantles and heating of the hot core. It has been suggested that the observed H₂O gas may also have been newly formed by reactions of atomic O and H₂ in warm conditions ($T > 200 \text{ K}$) in the central hot core or in shocks created by the outflow (e.g., van Dishoeck & Blake 1998). However, the total (gas plus ice) H₂O abundance decreases for the more evolved objects, indicating that H₂O is destroyed rather than being newly formed (van Dishoeck 1998). The low gas phase CO₂ abundance in all sources indicates that this molecule is destroyed even more efficiently after evaporation from the grains (Boonman et al. 2000; Charnley & Kaufman 2000).

In the proposed heating sequence, Elias 29 is placed after W 33A, and before GL 2591. However, the various ice band profiles (H₂O, CO, CO₂, and 6.85 μm) in Elias 29, indicate little thermal processing, resembling very much NGC 7538 : IRS9, rather than W 33A or GL 2591. The combination of high gas phase abundances and temperatures, together with a lack of signatures of thermal processing in the ice bands, as seen in Elias 29, is remarkable and is not seen in high mass protostars. Geometric effects may play an important role in the evolution of molecular envelopes around low mass protostars (see Sect. 4.2).

Whereas thermal evaporation can explain the abundance variations of volatiles such as H₂O, CO, CO₂, NH₃, and CH₄, other mechanisms are needed to explain the variations of solid CH₃OH, and XCN abundances among the sources in our sample (Table 3). It has been widely considered that XCN molecules are formed by energetic processing of icy grain mantles by stellar or cosmic ray induced far-ultraviolet radiation, or by bombardment with highly energetic particles (e.g. Lacy et al. 1984, Grim & Greenberg 1987, Allamandola et al. 1988). The high CH₃OH abundances toward sources with deep XCN bands, and the apparent absence of CH₃OH toward low mass protostars and dark clouds might suggest that the energetics of nearby massive stars is needed to produce CH₃OH (Gibb et al. 2000).

Table 4. Gas-to-solid state column density ratios

Object	CO ^a	H ₂ O ^a	CO ₂ ^a	T_{warm} ^b
Dark Cl.	<1	<0.02	–	–
N7538/9	12 (6)	<0.05	0.005	180 (40)
W 33A	45 (22)	<0.11	0.015	120 (20)
Elias 29	>53	>0.23	<0.011	1000 (500)
GL 2591	>400	2.4	0.17	1000 (200)

^a Determined from Table 3

^b Temperature of warm CO gas (Mitchell et al. 1990)

4.2. The structure of Elias 29

The variety of dust, gas and ice absorption and emission components presented here, and in the literature, allows us to construct an overall view of the structure of Elias 29. The scale on which the detected hot CO gas is present can be constrained when one assumes that the pure rotational high-J CO emission lines detected toward Elias 29 with ISO-LWS (Ceccarelli et al., in prep.) are emitted by the same hot gas. We fit these observed line fluxes, by assuming spontaneous, optically thin emission from an LTE level distribution, and leaving the size of the emitting region as a free parameter. For the range of column densities and temperatures found to fit the CO ab-

¹ For actual, local, abundances in high mass protostars we refer to Boonman et al. 2000

sorption lines (Fig. 11), we find diameters in the range 85–225 AU. Thus, the observed hot CO gas may be present in a hot core region with the size of a circumstellar disk. The gas could be concentrated in a high density photospheric layer above the disk. To sufficiently heat it by radiation from the central star, the disk needs to flare outwards, rather than being flat (e.g. Chiang & Goldreich 1997). We cannot exclude however that the gas is present more uniformly in the hot core, at lower densities. It might then also be partly heated by shocks from the outflow close to the star. A more detailed modeling of the CO emission lines, including departures from LTE, optical depth corrections, and taking into account excitation by radiative pumping, are needed to further confine the location of the gas phase CO and H₂O components (Ceccarelli et al., in prep.).

The lack of signatures of thermal processing in the ice bands, locates the ice in a region shielded from the central heating source. The ices could be present in a foreground cloud, an extended envelope, or a circumstellar disk seen close to edge-on. Millimeter wave continuum observations indicate an extended envelope, concentrated on the infrared source (FWHM=17"; 2600 AU; André & Montmerle 1994; Motte et al. 1998). For a wide range of power law model fits to the far-infrared SED, André & Montmerle find that the envelope mass is 0.1 M_{\odot} , with a volume averaged dust temperature of typically $T = 35$ K. This temperature is high enough to evaporate the most volatile, apolar ices, but too low to induce ice crystallization. Hence, indeed the observed H₂O, CO₂, and probably “6.85” μm ices could be associated with this extended envelope. Some of the apolar CO ice has evaporated in the envelope after the formation of the low mass protostar, as indicated by the significantly lower CO/H₂O ice ratio toward Elias 29, compared to other sight-lines with little thermal processing in the ices (NGC 7538 : IRS9, Elias 16; Table 3). In this picture, the detected apolar CO ice could thus be spatially separate from the other ices, perhaps in foreground clouds, or well shielded in a very cold disk.

Knowledge of the source structure is essential to interpret the observed solid and gas phase species. For example, if the ice is present in the disk, rather than in the envelope, we must see the disk in a near edge-on configuration. Is there independent evidence for the presence of a disk surrounding Elias 29 and what would be its orientation? The most direct view is provided by lunar occultation observations. A central object with diameter of ~ 1 AU emits 90% of the 2.2 μm continuum emission (Simon et al. 1987). The remaining 10% comes primarily from an object of 60 AU in diameter, which could be the hot part of a disk ($T \sim 1000$ K). The strongest spectroscopic disk indicator would be the presence of emission or absorption of vibrational overtone band heads of CO (e.g. Carr 1989; Najita et al. 1996). The 2.0–2.5 μm spectrum of Elias 29 does not show these features, in contrast to other protostars in ρ Oph, such as WL 16 (Greene &

Lada 1996). However, the absence of CO overtone bands does not prove the absence of an (inner) disk (Calvet et al. 1991). For example, the Herbig Ae object AB Aur does not have detected CO overtone bands, while high spatial resolution radio continuum and emission line observations provide strong evidence for the presence of a circumstellar disk around this object (Mannings & Sargent 1997).

AB Aur is an interesting comparison source, since it has the same luminosity as Elias 29 ($\sim 40 L_{\odot}$), and the SEDs of both objects are remarkably similar (Fig. 2). The flatness of the SED in AB Aur is well reproduced in flaring disk models, where the dust in the outer parts of the disk is more efficiently heated than in flat disks (Chiang & Goldreich 1997). The disk is optically thick up to 100 μm , and becomes optically thin at longer wavelengths where the SED drops steeply (e.g. van den Ancker et al. 2000). The similarity of the SEDs does however not necessarily imply that Elias 29 is dominated by an optically thick disk as well. A flat SED could also be produced by the envelope, if it has a shallow power law density profile (index ~ 0.5 ; André & Montmerle 1994). This density profile is remarkably flat compared to high mass protostars (van der Tak et al. 2000; Dartois et al. 1998a), and other low mass protostars (e.g. Hogerheijde & Sandell 2000). Finally, flat energy distributions are also created by the combination of a disk and envelope. Here, the heated envelope irradiates the outer parts of the disk (Natta 1993).

Without direct high resolution imaging, it is difficult to discriminate between these models. Assuming a given model however, the present observations put some constraints. In the disk scenario, its orientation would have to be closer to edge-on than face-on to explain the absorption line spectrum of Elias 29 (Chiang & Goldreich 1999). In these models, an inclination larger than $\sim 70^{\circ}$ can however be excluded, because this would give an SED that peaks in the far-infrared, in contrast to what is observed for Elias 29. Also, if the disk were edge-on, a higher absorbing column, perhaps an order of magnitude larger than the observed $N_{\text{H}} \sim 1.2 \times 10^{23} \text{ cm}^{-2}$ (Sect. 3.2) would be expected (Sekimoto et al. 1997). An independent measure for N_{H} and the disk inclination is provided by the hard X-ray flux and spectrum, arising from hot gas in the magnetosphere. For Elias 29, a high $N_{\text{H}} \sim 2 \times 10^{23} \text{ cm}^{-2}$ is observed during X-ray flares, but N_{H} is a factor of 5 lower in quiescent phases (Kamata et al. 1997). Perhaps the X-ray flares are formed low in the magnetosphere, and in the relatively high inclination of the disk, they trace higher column densities compared to X-rays formed in quiescent phases higher in the magnetosphere.

5. Conclusions and future work

The 1.2–195 μm spectrum of the low mass protostellar object Elias 29 in the ρ Ophiuchi molecular cloud shows a wealth of absorption lines of gas and solid state molecules.

Hot CO and H₂O gas are detected ($T_{\text{ex}} > 300$ K) at rather high abundances, on scales of not more than a few hundred AU. The ice abundances are relatively low. In this respect, Elias 29 resembles luminous protostars with significantly heated cores, such as GL 2591. However, *none* of the many ice bands that are detected, i.e. from H₂O, CO, CO₂, and the 6.85 μm band, shows outspoken signs of thermal processing. Again in comparison with luminous protostars, Elias 29 now resembles less evolved objects, such as NGC 7538 : IRS9. Our combined gas and solid state analysis thus shows that high and low mass protostars heat their molecular envelopes in different ways. This may be related to their different structure, such as the presence of a circumstellar disk in low mass protostars. The hot gas of Elias 29 could be present on the surface of a flaring disk, which is efficiently heated by the central star. The ices toward Elias 29 must be well shielded in a circumstellar disk seen close to edge-on, or far away in the envelope.

Does this imply that in general the ices in the disks or outer envelopes of low mass protostars remain unaltered, both in composition and structure, during the process of star formation? Are these ices the building blocks of the early solar system and are they preserved in present day observed cometary nuclei? To date, no Class I protostar has been found with strong signs of crystalline ices (Boogert et al. 2000). On the other hand, the presence of crystalline ices and silicates has been reported in several isolated, less embedded Herbig Ae/Be objects (Malfait et al. 1999). This research needs to be extended to a larger sample of low mass protostars, in a range of evolutionary stages and luminosities. Furthermore, it is essential for the interpretation of the gas and solid state characteristics toward Elias 29 that the presence of a circumstellar disk, and its inclination are determined by future high spatial resolution infrared or millimeter continuum observations.

Acknowledgements. We thank Tom Greene (NASA/Ames Research Center) for providing us the 1.1–2.4 μm spectrum of Elias 29 in electronic format, Willem Schutte (Leiden Observatory) for providing the H₂O:NH₃ laboratory ice mixtures, and T.Y. Brooke (NASA/JPL) for the 3 μm spectrum of NGC 7538 : IRS9. The referee D. Ward-Thompson is thanked for a number of useful comments. D.C.B.W. is funded by NASA through JPL contract no.961624 and by the NASA Exobiology and Long-Term Space Astrophysics programs (grants NAG5-7598 and NAG5-7884, respectively).

References

- Adams F.C., Lada C.J., Shu F.H., 1987, ApJ 312,
 Allamandola L.J., Sandford S.A., Valero G.J., 1988, Icarus 76,
 225
 Allamandola L.J., Sandford S.A., Tielens A.G.G.M., Herbst
 T.M., 1992, ApJ 399, 134
 André Ph., Montmerle Th., 1994, ApJ 420, 837
 André Ph., Ward-Thompson D., Barsony M., 1993, ApJ 406,
 122
 Bohlin R.C., Savage B.D., Drake J.F., 1978, ApJ 224, 132
 Bohren C.F., Huffman D.R., 1983, Absorption and Scattering
 of Light by Small Particles. John Wiley & Sons, New York,
 App. B
 Bontemps S., André P., Terebey S., Cabrit S., 1996, A&A 311,
 858
 Boogert A.C.A., Schutte W.A., Tielens A.G.G.M., et al., 1996,
 A&A 315, L377
 Boogert A.C.A., Helmich F.P., van Dishoeck E.F., et al., 1998,
 A&A 336, 352
 Boogert A.C.A., Ehrenfreund P., Gerakines P.A., et al., 2000,
 A&A 353, 349
 Boonman A.M.S., van Dishoeck E.F., Doty S.D., et al., 2000,
 A&A, subm.
 Brooke T.Y., Sellgren K., Smith R.G., 1996, ApJ 459, 209
 Brooke T.Y., Sellgren K., Geballe T.R., 1999, ApJ 517, 883
 Calvet N., Patino A., Magris G.C., d’Alessio P., 1991, ApJ 380,
 617
 Carr J.S., 1989, ApJ 345, 522
 Caux E., Ceccarelli C., Castets A., et al., 1999, A&A 347, L1
 Charnley S.B., Kaufman M.J., 2000, ApJ 529, 111
 Chen H., Myers P.C., Ladd E.F., Wood D.O.S., 1995, ApJ 445,
 377
 Chiang E.I., Goldreich P., 1997, ApJ 490, 368
 Chiang E.I., Goldreich P., 1999, ApJ 519, 279
 Chiar J.E., Adamson A.J., Kerr T.H., Whittet D.C.B., 1995,
 ApJ 455, 234
 Chiar J.E., Adamson A.J., Whittet D.C.B., 1996, ApJ 472, 665
 Chiar J.E., Gerakines P.A., Whittet D.C.B., et al., 1998, ApJ
 498, 716
 Chiar J.E., Tielens A.G.G.M., Whittet D.C.B., et al., 2000,
 ApJ 537, in press
 Clegg P.E., Ade P.A.R., Armand C., et al., 1996, A&A 315,
 L38
 Dartois E., Cox P., Roelfsema P.R., et al., 1998a, A&A 338, 21
 Dartois E., d’Hendecourt L., Boulanger F., et al., 1998b, A&A
 331, 651
 Dartois E., Schutte W., Geballe T.R., et al., 1999, A&A 342,
 32
 de Graauw Th., Haser L.N., Beintema D.A., et al., 1996, A&A
 315, L49
 d’Hendecourt L.B., Allamandola L.J., 1986, A&AS 64, 453
 Draine B.T., Lee H.M., 1984, ApJ 285, 89
 Ehrenfreund P., Boogert A.C.A., Gerakines P.A., Tielens
 A.G.G.M., van Dishoeck E.F., 1997, A&A 328, 649
 Elias J.H., 1978, ApJ 224, 857
 Elsila J., Allamandola L.J., Sandford S.A., 1997, ApJ 479, 818
 Gerakines P.A., Schutte W.A., Greenberg J.M., van Dishoeck
 E.F., 1995, A&A 296, 810
 Gerakines P.A., Whittet D.C.B., Ehrenfreund P., 1999, ApJ
 522, 357
 Gibb E.L., Whittet D.C.B., Schutte W.A., et al., 2000, ApJ,
 in press
 Gillett F.C., Forrest W.J., Merrill K.M., Soifer B.T., Capps
 R.W., 1975, ApJ 200, 609
 Gonzalez-Alfonso E., Cernicharo J., van Dishoeck E.F., Wright
 C.M., Heras A., 1998, ApJ 502, L169
 Goorvitch D., 1994, ApJS 95, 535
 Greene Th.P., Lada C.J., 1996, AJ 112, 2184
 Greene Th.P., Lada C.J., 2000, AJ, in press
 Grim R.J.A., Greenberg J.M., 1987, ApJ 321, L91

- Hanner M.S., Brooke T.Y., Tokunaga A.T., 1995, *ApJ* 438, 250
- Helmich F.P., 1996, Ph. D. thesis. Rijksuniversiteit Leiden
- Helmich F.P., van Dishoeck E.F., Black J.H., et al., 1996, *A&A* 315, L173
- Hillenbrand L.A., Strom S.E., Vrba F.J., Keene J., 1992, *ApJ* 397, 613
- Hogerheijde M.R., Sandell G., 2000, *ApJ*, in press
- Hudgins D.M., Sandford S.A., Allamandola L.J., Tielens A.G.G.M., 1993, *ApJS* 86, 713
- Ivezic Z., Elitzur M., 1997, *MNRAS* 287, 799
- Kamata Y., Koyama K., Tsuboi Y., Yamauchi S., 1997, *PASJ* 49, 461
- Keane J.V., Tielens A.G.G.M., Boogert A.C.A., Schutte W.A., Whittet D.C.B., 2000, *A&A*, in press
- Kerkhof O., Schutte W.A., Ehrenfreund P., 1999, *A&A* 346, 990
- Kerr T.H., Adamson A.J., Whittet D.C.B., 1993, *MNRAS* 262, 1047
- Kessler M.F., Steinz J.A., Anderegg M.E., et al., 1996, *A&A* 315, L27
- Lacy J.H., Baas F., Allamandola L.J., et al., 1984, *ApJ* 276, 533
- Lacy J.H., Knacke R., Geballe T.R., Tokunaga A.T., 1994, *ApJ* 428, L69
- Lacy J.H., Faraji H., Sandford S.A., Allamandola L.J., 1998, *ApJ* 501, 105
- Lada C.J., Wilking B.A., 1984, *ApJ* 287, 610
- Lahuis F., van Dishoeck E.F., 2000, *A&A* 355, 699
- Leech K., 2000, *The ISO handbook*, vol.VI: SWS, http://isowww.estec.esa.nl/manuals/handbook/vi/sws_hb/, p.132
- Léger A., Gauthier S., Defourneau D., Rouan D., 1983, *A&A* 117, L164
- Liseau R., Olofsson G., 1999, *A&A* 343, L83
- Loren R.B., Wootten A., Wilking B.A., 1990, *ApJ* 365, 269
- Maldoni M.M., Smith R.G., Robinson G., Rookyard V.L., 1998, *MNRAS* 298, 251
- Malfait K., Waelkens C., Bouwman J., de Koter A., Waters L.B.F.M., 1999, *A&A* 345, 181
- Mannings V., 1994, *MNRAS* 271, 587
- Mannings V., Sargent A.I., 1997, *ApJ* 490, 792
- Martin P.G., Whittet D.C.B., 1990, *ApJ* 357, 113
- Mitchell G.F., Maillard J.-P., Allen M., Beer R., Belcourt K., 1990, *ApJ* 363, 554
- Mitchell G.F., Maillard J.-P., Hasegawa T.I., 1991, *ApJ* 371, 342
- Motte F., André Ph., Neri R., 1998, *A&A* 336, 150
- Najita J., Carr J.S., Tokunaga A.T., 1996, *ApJ* 456, 292
- Natta A., 1993, *ApJ* 412, 761
- Palla F., Stahler S.W., 1993, *ApJ* 418, 414
- Palumbo M.E., Geballe T.R., Tielens A.G.G.M., 1997, *ApJ* 479, 839
- Pendleton Y.J., Tielens A.G.G.M., Werner M.W., 1990, *ApJ* 349, 107
- Pendleton Y.J., Tielens A.G.G.M., Tokunaga A.T., Bernstein M.P., 1999, *ApJ* 513, 294
- Roche P.F., Aitken D.K., 1984, *MNRAS* 208, 481
- Rothman L.S., Gamache R.R., Tipping R.H., et al., 1992, *J. Quant. Spectrosc. Radiat. Transfer* 48, 469
- Sandford S.A., Allamandola L.J., 1993, *ApJ* 417, 815
- Saraceno P., André P., Ceccarelli C., Griffin M., Molinari S., 1996, *A&A* 309, 827
- Schutte W.A., Tielens A.G.G.M., Sandford S.A., 1991, *ApJ* 382, 523
- Schutte W.A., Tielens A.G.G.M., Whittet D.C.B., et al., 1996, *A&A* 315, 333
- Schutte W.A., van der Hucht K.A., Whittet D.C.B., et al., 1998, *A&A* 337, 261
- Sekimoto Y., Tatematsu K., Umemoto T. et al., 1997, *ApJ* 489, L63
- Simon M., Howell R.R., Longmore A.J., et al., 1987, *ApJ* 320, 344
- Skinner C.J., Tielens A.G.G.M., Barlow M.J., Justtanont K., 1992, *ApJ* 399, 79
- Smith R.G., Sellgren K., Tokunaga A.T., 1989, *ApJ* 344, 413
- Smith R.G., Sellgren K., Brooke T.Y., 1993, *MNRAS* 263, 749
- Swinyard B.M., Clegg P.E., Ade P.A.R., et al., 1996, *A&A* 315, L43
- Tanaka M., Sato S., Nagata T., Yamamoto T., 1990, *ApJ* 352, 724
- Tegler S.C., Weintraub D.A., Rettig T.W., et al., 1995, *ApJ* 439, 279
- Tielens A.G.G.M., 1982, Ph. D. thesis. Rijksuniversiteit Leiden
- Tielens A.G.G.M., Tokunaga A.T., Geballe T.R., Baas F., 1991, *ApJ* 381, 181
- van den Ancker M.E., Bouwman J., Wesselius P.R., et al., 2000, *A&A*, in press
- van der Tak F.F.S., van Dishoeck E.F., Evans N.J. II, Bakker E.J., Blake G.A., 1999, *ApJ* 522, 991
- van der Tak F.F.S., van Dishoeck E.F., Evans N.J. II, Blake G.A., 2000, *ApJ*, in press
- van Dishoeck E.F., 1998, *Faraday Discussions* 109, 31
- van Dishoeck E.F., Blake G.A., 1998, *ARAA* 36, 317
- van Dishoeck E.F., Helmich F.P., de Graauw Th., et al., 1996, *A&A* 315, L349
- Whittet D.C.B., 1974, *MNRAS* 168, 371
- Whittet D.C.B., Schutte W.A., Tielens A.G.G.M., et al., 1996, *A&A* 315, L357
- Whittet D.C.B., Gerakines P.A., Tielens A.G.G.M., et al., 1998, *ApJ* 498, L159
- Wilking B.A., Lada C.J., 1983, *ApJ* 271, 698
- Wilking B.A., Lada C.J., Young E.T., 1989, *ApJ* 340, 823
- Willner S.P., Gillet F.C., Herter T.L., et al., 1982, *ApJ* 253, 174
- Young E.T., Lada C.J., Wilking B.A., 1986, *ApJ* 304, L45